Micro-Hardness and Strain-Rate-Dependent Compressive Response of an Ultra-Light-Weight Mg-Li-Al Alloy

Haoyang Li[a,*], Chenwei Shao[b], David Funes Rojas[c], Mauricio Ponga[c,**], James D. Hogan[a]

[a]*Department of Mechanical Engineering, University of Alberta, Edmonton, AB T6G 2R3, Canada*
[b]*Laboratory of Fatigue and Fracture for Materials, Institute of Metal Research, Chinese Academy of Sciences, Shenyang 110016, People's Republic of China*
[c]*Department of Mechanical Engineering, University of British Columbia Vancouver Campus, BC V6T 1Z4, Canada*

Abstract

A study on the microstructure and composition, micro-hardness and strain-rate-dependent compressive behaviors, and the associated failure mechanisms of an ultra-light-weight Mg-Li-Al alloy were conducted. X-ray diffraction and X-ray photoelectron spectroscopy showed a multi-phase material with $\sim$ 35 wt% Li and $\sim$ 20 wt% Al, and a dendritic "fishbone" microstructure was resulting from the high percentage of both Li and Al. Micro-indentation measurements showed a superior hardness (1.63 $\pm$ 0.08 GPa) that is > 1.5x higher than Mg-Li-Al alloys reported in the literature, with a low density ($\sim$ 1.68 g/cm^3) comparable to Mg alloys. Strain-rate-dependent uniaxial compression experiments demonstrated no strain-rate-sensitivity in the peak strength (699.4 $\pm$ 74.0 MPa) at strain rates between 10^{-5} and 10^3 s^{-1}. High-speed imaging revealed a shear-mode brittle fracture under both quasi-static and dynamic conditions, with an additional splitting crack mechanism observed under dynamic loading. Crack propagation speeds demonstrated a positive correlation with strain rate from $\sim$ 480 m/s at $\sim$ 100 s^{-1} to $\sim$ 1000 m/s at $\sim$ 2000 s^{-1}. Post-mortem analysis showed that the "fishbone" structure with a peeling fracture mechanism appears to be the dominant site promoting shear failure across all strain rates.

Keywords: Mg-Li-Al, ultra-light-weight, XPS, strain-rate-dependent uniaxial compression, SHPB, micro-hardness, compressive strength, failure mechanisms

---

*Corresponding author
**Corresponding author
Email addresses: `haoyang@ualberta.ca` (Haoyang Li), `mponga@mech.ubc.ca` (Mauricio Ponga)

1. Introduction

The magnesium-lithium-based (Mg-Li-X) alloys have attracted significant attention from industrial and scientific communities due to their potential for significant weight reduction while maintaining good mechanical properties (e.g., high specific strength and stiffness) [1–4]. The combination of two light elements, Mg (~ 1.74 g/cm^3) and Li (~ 0.54 g/cm^3), could produce alloys that have densities between 1.3 and 1.7 g/cm^3 [5], which are about 50% of the Al-based alloys. The decrease in density will decrease energy consumption and, for example, reduce green-house gases emissions of transportation vehicles [5, 6]. Combining the low-density high-strength alloys with appropriate coatings can potentially improve fuel efficiency in aerospace and space missions, while preserving sufficient strength for structural integrity from debris impact [7]. In addition, alloying Mg (hexagonal closed pack (HCP) crystal structure) with Li (body center cubic (BCC) crystal structure) can improve the ductility and formability of the Mg-based alloys [8]. However, pure Mg-Li alloys suffer from low absolute engineering strength (a trade-off from adding Li), where improvements are sought to be made through adding other alloying elements like Al, Zn, and Ca [9–11].

Among the Mg-Li-X family, the Mg-Li-Al ultra-light-weight alloy has been well explored due to the claimed strengthening effect introduced by Al, while preserving a similar density as the Mg-Li matrix [12–15]. The initial studies of Mg-Li-Al alloys showed limited progress in solving the microstructural instability during fabrication [16–18] and unraveling the coupling effect of adding Al and Li on the resulting microstructure and mechanical performance [19, 20]. Past efforts have been mainly focusing on generating the phase diagram of the Mg-Li-Al system [21, 22]. The phase diagram indicates that different phase structures can be formed with respect to the lithium content [22]: pure α-HCP structure with Li content less than 5.7 wt%; duplex (α-HCP + β-BCC) structure with Li content between 5.7 and 10.3 wt%; and pure β-BCC structure with Li content higher than 10.3 wt% [22]. This concept has been commonly adapted by industries and researchers when developing Mg-Li-based alloys [17, 23]. Building on these works, post-processing methods, such as solution treatment [10], severe plastic deformation (SPD) [24], aging [12], water quenching [25], and rolling [26] were applied to modify the microstructure (e.g. secondary phase precipitation [27, 28], grain refinement [29]), and mechanical properties (e.g., ductility [30]).

In addition to processing effects on microstructure, numerous studies evaluated the mechanical performance of Mg-Li-Al alloys and showed very different behaviors (e.g., hardness [31, 32], strength [13, 33], ductility [24, 34], and fracture toughness [35]). Tensile testing under quasi-static conditions is often used to evaluate the strength and elongation of the materials [9, 11, 12, 15, 24, 25, 36]. In some studies on Mg-Li-Al alloys, quasi-static compression testing have been carried out [12, 28, 33, 37]. For example, Zou et al. [8] found that the production of duplex phases and fine intermetallic particles through tuning the Li content could change the material ductility from < 20% to > 50%. In the studies by Islam et al. [31, 38], the stress-strain exhibited a sharp work-hardening stage followed by a dynamic recovery stage with softening

behavior.

Among all studies we have reviewed on the Mg-Li-Al system, some general trends have emerged: first, the Mg-Li-Al alloys can show vastly different mechanical behaviors under compression, such as from brittle to super-plastic behaviors [12]; second, the mechanical properties can vary across a wide range (e.g., peak strength can have more than an order difference) [28, 32]; and third, the microstructure-associated mechanisms in a given material could be entirely different because of the various phase structures present in the materials [16, 24]. With this in mind, this study explores a compositionally complex Mg-($\sim$ 35 wt%)Li-($\sim$ 20 wt%)Al alloy with detailed microstructure characterization and comprehensive strain-rate-dependent uniaxial compression testing. The microstructures of the as-received and tested materials are investigated using scanning electron microscopy. X-ray diffraction and X-ray photoelectron spectroscopy are used to identify phases and elemental compositions within the alloy. Next, micro-hardness of the material is measured and compared with other Mg-Li-Al alloys in the literature. Compressive mechanical response (i.e., stress-strain and the associated properties) are then obtained at strain rates between 10^{-5} and 10^3 s^{-1}, coupled with high-speed imaging. To the authors' best knowledge, first, the composition of this studied Mg-Li-Al alloy has never been reported in the literature, which results in extraordinary mechanical properties (i.e., compressive strength, density, and hardness); and second, very limited data-sets are available for dynamic mechanical testing on similar Mg-Li-Al alloys [39]. Our study opens up the possibility to explore ultra-light-weight compositionally complex alloys based on near-equiatomic compositions with Mg, Li and Al.

2. Materials and Experimental Method

2.1. Materials

The Mg-Li-Al alloy was fabricated by American Elements (Los Angeles, California, USA) in solid disks (100 mm in diameter x 8 mm in thickness). The Mg, Li, and Al were pre-mixed equi-atomically, melted in a Ar gas controlled environment, and cooled down quickly to avoid diffusion of the elements. However, fabrication details remain a trade secret with the company and cannot be disclosed. Here, we point out the trace elements reported from the manufacturer for the reader's interest: Fe (0.0015%), Zn (0.0006%), Si (0.0008%), Ti (0.0003%), Cu (0.0012%), and Ni (0.0002%). Samples used in testing were electron discharge machined (EDM) from the solid disks into cubes and mechanically polished to less than 0.1 μm RA. Nominal sample dimensions for compression testing were 5.0 mm x 4.5 mm x 3.5 mm, with the 5.0 mm edge parallel to the cast direction. The sample orientation is defined in Figure 1, where ND and PD denote the "normal-to-cast" and "parallel-to-cast" directions, respectively. All tests were carried out in the PD direction (along the 5 mm edge). All samples were checked with tolerances within 1% error in each dimension (e.g., 5.00$\pm$ 0.05 mm) and 0.05° in parallelism before testing. For characterization on the intact material, one of the surfaces

is further polished to remove the built-up oxidized layer and chemically etched in a 3% HBF_4 solution for two seconds to better reveal the microstructure during microscopy.
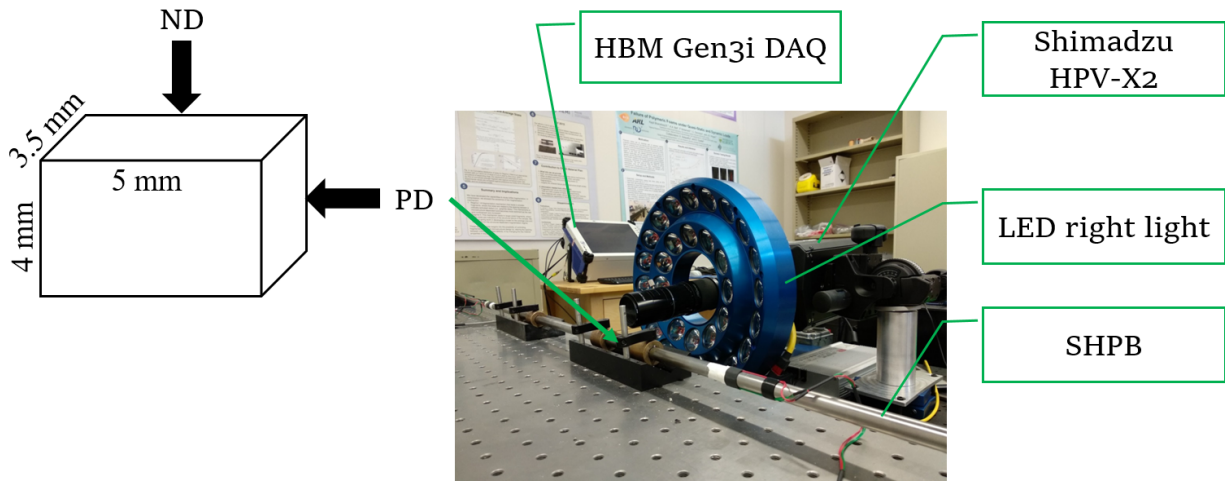

Figure 1: Split-Hopkinson pressure bar setup for dynamic testing with an ultra-high-speed camera, LED ring light, and high-speed data acquisition system. The insert on the left shows the sample dimensions and orientation. ND and PD denote the "normal-to-built" and "parallel-to-built" directions, respectively. All testing are done along the PD direction.

2.2. Scanning Electron Microscopy

Scanning electron microscopy (SEM) was carried out using a Zeiss Sigma FESEM machine equipped with an energy-dispersive X-ray spectroscopy (EDS) setup. The machine was operated with the acceleration voltage set at 20 kV and a working distance of $\sim$ 8.5 mm. Micrographs were obtained using both In-Lens and secondary electron (SE) detectors. The EDS data was analyzed using the AZtec software from Oxford Instruments. SEM was utilized to study both intact material microstructures and post-mortem failure mechanisms, with EDS being used to confirm the element distribution. Note that Lithium cannot be detected using EDS because it is a light element close to hydrogen, and so X-ray diffraction and X-ray photoelectron spectroscopy were employed to study the phase and chemical composition of the material (details forthcoming).

2.3. X-ray Diffraction

X-ray diffraction (XRD) was used to determine the phases present in the material. XRD spectrums were obtained using a Bruker D8 Discover system equipped with a Cu Kα beam source and a high throughput LynxEYE 1-dimensional detector. The 1-D diffraction spectrum was obtained using a scan rate of $1.5°$/min, a step size of $0.015°$, and a scanning range between 20 and $90°$. The 2θ range was chosen by surveying literature and identifying the possible phases that could be present in the Mg-Li-Al alloys [17, 33]. The apparatus was operated at 40 kV and 30 mA on a standard stage, and the 2θ-θ spectrum was obtained using

the COMMANDER software. Three spectrum were acquired from different samples to check repeatability. Finally, the phases were matched using the JADE software with the K-α_2 background signal removed, and the theoretical spectrum from Materials Project archive [40] was used to confirm the matches.

2.4. X-ray Photoelectron Spectroscopy

X-ray photoelectron spectroscopy (XPS) was used to determine the sub-surface chemical composition (~ 10 nm depth profile) of the studied Mg-Al-Li alloy. The scan was conducted on a PHI VersaProbe III Scanning XPS Microprobe machine with an Al Kα source (100.60 W) at a beam voltage of 20 kV. Argon ion sputtering with a sputtering energy of 2 kV was applied for 2.5 minutes before scanning to remove environmental contagions (~ 20 nm removal) and reduce signal noise. Post-processing of the binding energy spectrum was carried out on the CasaXPS software to identify the characteristic peaks and estimate the atomic percentage of the Mg, Li, and Al elements. The atomic percentages were then converted to weight percentage.

2.5. Micro-Hardness Testing

The Vickers hardness of the studied Mg-Li-Al alloy was measured using a Wilson VH1102 micro-hardness tester (Buehler Wilson, Illinois, USA) following ASTM C1327 [41]. Indentations were carried out on both 5.0 x 4.0 mm^2 (PD direction) and 3.5 x 4.0 mm^2 (ND direction) surfaces. Each indent was made with a 200g load applied over a dwell time of 15 seconds. In total, at least 10 valid measurements were performed on each surface, and the average value and standard deviation were obtained. The validity of the measurements was checked by taking the diagonal differences to be less than 5%. Vickers hardness measurements (in HV) were converted to GPa for better comparison with literature.

2.6. Strain-Rate-Dependent Uniaxial Compression Testing

Quasi-static compression tests were performed on a servo-hydraulic MTS 810 load frame. A detailed description and the schematic can be found in a previous study [42]. All testing was done along the PD direction (5.0 mm edge). The machine was set to displacement control with nominal displacement rates of 0.0005 mm/s, 0.005 mm/s, 0.05 mm/s, and 0.5 mm/s, resulting in nominal strain rates of $\sim 5 \times 10^{-5}$ s^{-1}, $\sim 5 \times 10^{-4}$ s^{-1}, $\sim 5 \times 10^{-3}$ s^{-1}, $\sim 5 \times 10^{-2}$ s^{-1}. In this study, we consider strain rates less than 1 s^{-1} to be quasi-static. The engineering stress was calculated by dividing the load cell outputted force by the cross-sectional area (3.5 x 4.0 mm^2). A U750 Promon camera with a full resolution of 1280 x 1024 pixel^2 (actual resolution of ~ 630 x 590 pixel^2 after zooming in on the samples) was used to visualize the specimen surface and record frames for later two-dimensional Digital Image Correlation analysis (2D-DIC). All strain (engineering) information is extracted from DIC, and the strain rate was estimated using the strain-time history.

Dynamic compression experiments were conducted using a modified split-Hopkinson pressure bar (SHPB) system, which is the same setup in [42]. All bars (incident, transmitted, and striker) in the current system are made of hardened C-350 maraging steel (E = 200 GPa, σ_y = 2.36 GPa) with a common diameter of 12.7 mm. The striker, incident, and transmitted bars are 304 mm, 1016 mm, and 916 mm long, respectively. From the quasi-static tests and micro-hardness measurements, protective platens were not needed because the strength (< 1 GPa) and hardness ($\sim$ 1.7 GPa) of the studied alloy were much lower than those of the bars (σ_y > 2 GPa and Hv > 7 GPa). High pressure grease was applied at the bar-sample interfaces to reduce friction and allow for free lateral expansion. Here, we acknowledge the limitations of using cubic samples compared to cylindrical and dumbbell samples in terms of stress concentration reduction and stress equilibrium [43–46]. In this study, cubic samples (dimensions: 3.5 x 4.0 x 5.0 mm^3) were used to compensate for the diameter of the split-Hopkinson pressure bar and facilitate two-dimensional Digital Image Correlation measurements, including axial, lateral, and shear strains (see Section 2.6), and crack propagation speed measurements. For imaging, a Shimadzu HPV X-2 ultra-high-speed camera with a full resolution of 400 x 250 pixel^2 (actual resolution 250 x 200 pixel^2) equipped with a K2 DistaMax Infinity lens was used to image the sample surface for deformation and DIC analysis. Imaging lighting was enhanced by using a REL, Inc. LED high-power ring light. An HBM Gen3i High-Speed Recorder was employed for data acquisition at 4 MHz with a Bessel IIR pre-filter to eliminate low frequency noise, and this well-exceeded the sampling frequency needed to compensate for the Nyquist rate. The engineering stress-time history for each experiment was computed using the signal from the transmitted gauge mounted on the SHPB. Similar to the quasi-static experiments, all engineering strain and strain rate information are obtained using DIC.

In this study, we considered strain rates greater than 10 s^{-1} to be dynamic. For the dynamic compression tests, we were able to achieve ranging strain rates by changing pulse shapers and impact velocities. As a result, three distinct strain rate regimes were accessed, with the strain rate ranging between 80 and 2200 s^{-1}. Specifically, strain rates between 80 and 150 s^{-1} were achieved by using tin pulse shapers (1.59 mm = 1/16 inches in thickness and 3.97 mm = 5/32 inches in diameter) and various pressures, whereas strain rates between 400 and 600 s^{-1} were reached with mild steel pulse shapers (0.79 mm = 1/32 inches in thickness and 3.175 mm = 1/8 inches in diameter), and between 1700 and 2200 s^{-1} were accomplished with paper pulse shapers (0.1 mm = 0.004 inches in thickness and 3.97 mm = 5/32 inches in diameter) or no pulse shapers. These pulse shaping configurations were found to produce signals with low fluctuations and proper rise times that allow the samples to fail in a single pass of a compressive wave, while maintaining good equilibrium and force balance. In this study, we conducted at least three repeated quasi-static experiments and five repeated dynamic experiments at each strain rate.

Lastly, we provide a brief summary of the DIC technique, where a detailed setup of DIC can be found in a previous study by the authors [47]. In this study, 2D-DIC was employed as a non-destructive computer-vision

strain measurement technique in all compression tests, and it has been proven reliable on other brittle solids under various loading conditions, including compression [48–52]. For all the compression experiments studied here, we were able to achieve a consistently low error, corresponding to correlation confidence intervals within the range of 10^{-2} to 10^{-3} pixels in quasi-static tests and 10^{-3} to 10^{-4} pixels in dynamic tests. Here, higher camera resolution results in higher cumulative error because of more seed points to match. This led to the total experimental measurement error in strain of $< 3\%$, accounting for tolerance in dimensions. The data analysis was done using the VIC-2D (v6 2018) software from Correlated Solutions (Irmo, South Carolina, USA), and the area of interest (AOI) was always defined for the entirety of the imaged sample surface to obtain average strain information. The subset (i.e., between 35x35 and 51x51 pixel^2 for quasi-static testing, and between 17x17 and 25x25 pixel^2 for dynamic testing) and step sizes (between 3 and 7 steps) were modified based on the minimization of the correlation error across the whole interrogated surface. No further post-filtering and time-smoothing was performed. After analysis, the 1-D average engineering axial strain-time history was extracted to match with the stress-time profile obtained from the testing setups. Strain equilibrium was checked by comparing strain-time histories of the local and global subsets, as detailed in Lo et al. [53], and an excellent match was obtained. This verified the use of average strain-time history and inferred the homogeneous deformation process.

3. Results

3.1. Material Characterization Using SEM, XRD, and XPS

First, SEM was used on the etched material surface to obtain information on the microstructure. The global micrograph of Figure 2 (a) shows two distinct phases present in the material. The brighter phase distributes heterogeneously in the material, with some high aspect ratio and discontinued particles dispersed randomly in the microstructure. In most regions of the brighter phase, the structure appears to be connected to form dendritic "fishbone" shape skeletons. Similar skeleton-like structures were reported in the literature for the Mg-Li-based system [17, 23, 29] and other systems, such as the Al-Ni [54] and Zn-Al [55] alloys. For example, at the bottom left of the micrograph, a clear signature of the "fishbone" structure indicates the brighter phase tends to grow and form an architecture in the material. The "fishbone" structure is usually encompassed by the darker phase as the matrix. The back-scattered SEM in Figure 2 (b) demonstrates a magnified view of the "fishbone" structure, where the structure extends horizontally in the micrograph. The single "fishbone" structure reveals a main frame in the middle, while high densities of branches intersect normally to the main frame but do not extend further beyond $\sim 30~\mu$m. The main frame is believed to dictate the major crystal growth direction of the brighter phase as similar dendrite growth behavior has been studied in [56] and [57].
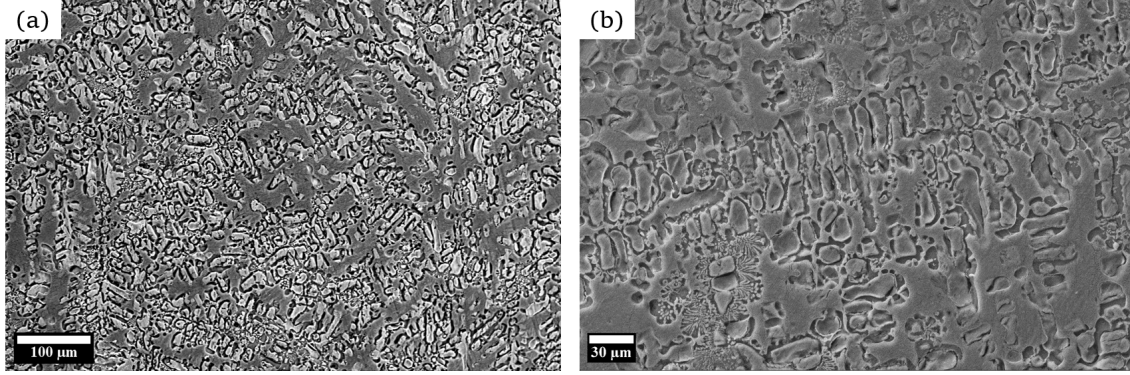
7

Figure 2: (a) Secondary electron and (b) back-scattered SEM micrographs showing two distinct phases present in the material, where the brighter phase in (a) distributes heterogeneously in the image. The shape of the brighter phase appears random (but mostly with high aspect ratios) in some areas, but it emerges as a dendritic "fishbone" structure in other regions (see bottom left and right of (a)). A magnified view on the "fishbone" microstructure in (b) demonstrates the dendrite growth direction of the brighter phase during solidification.

Next, XRD was conducted to investigate the phases and identify what each of the brighter and darker regions are in the microstructure. Shown in Figure 3 is the 1-D XRD spectrum of the studied Mg-Li-Al alloy with 2θ ranges from 20 to 90°. Numerous peaks appeared on the spectrum, with some convoluted peaks such as the ones at $\sim 37°$ and $\sim 63°$. The peaks are identified to our best knowledge by using both the JADE software and databases from Materials Project [40]. A multi-phase material is confirmed as expected, and the BCC β-Li, LiAl (with a BCC structure), and $MgLiAl_2$ constitute the major phases in the material. In addition, a peak for Li_2Mg is marked with the convoluted β-Li peak at $\sim 63°$, but it is minor compared to the major LiAl phase.

Next, SEM coupled with EDS mapping was carried out on a magnified microstructure of the "fishbone" skeleton and the surrounding area in order to identify the phase layout from XRD analysis (see Figure 4). It is observed that the "fishbone" structures contain high concentrations of the Al element (see Al map), while the surrounding areas have high concentrations of the Mg element (see Mg map). The distinct separation of Al- and Mg-rich regions indicates the possible location of the phases identified in the XRD spectrum, where the Al-rich regions ("fishbone" structures) could be a combination of LiAl and $MgLiAl_2$ phases [5, 28]. The $MgLiAl_2$ phase will likely be at the edge of the "fishbone" branches, given the co-existence of both Al and Mg elements. Therefore, the main frame of the "fishbone" is likely the LiAl phase, as well as the center of the individual branches along the main frame. This is similar to what has been observed in Li et al. [23] in Mg-(9 wt%)Li-(6 wt%)Al and Mg-(15 wt%)Li-(6 wt%)Al alloys. Further, the surrounding regions of the "fishbone" that consist of high concentrations of the Mg element are identified as mainly Li_2Mg and $MgLiAl_2$. Finally, note here that the Li element cannot be detected using the EDS technique, and we cannot know the exact location of the element. However, it is reasonable to assume that Li is highly-concentrated
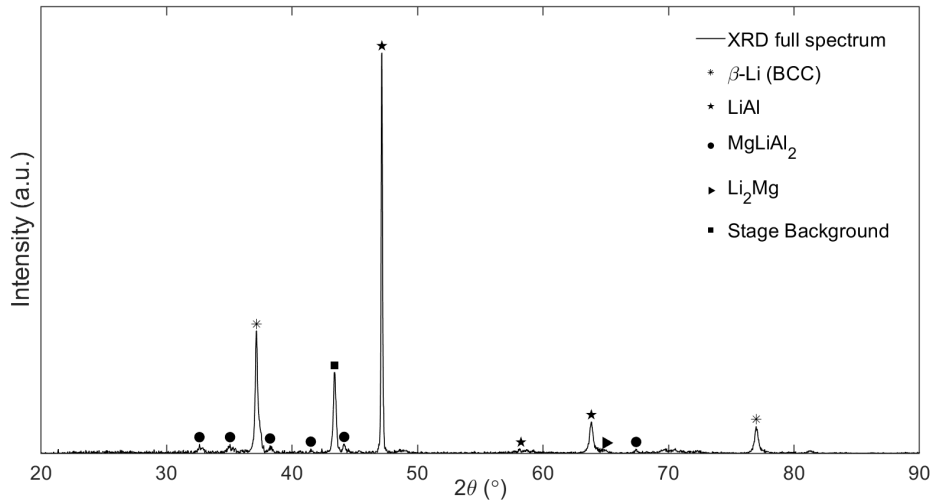
8

Figure 3: XRD spectrum of the Mg-Li-Al alloy revealing a multi-phase material, including a major peak for LiAl phase and multiple peaks for BCC β-Li. Another major phase is MgLiAl$_2$, which could also be shown in the Al-concentrated regions in the EDS maps. The machine stage background peaks are included for completeness.

on the Al-rich "fishbone" structures deducted from the atomic ratio of the present phases (see Figure 3). In addition, the O map in Figure 4 shows a much higher concentration of oxygen present in the Mg-rich regions compared to the Al-rich regions, and this can be the result of the higher oxidizing rate in Mg [58], or the formation of oxide compounds in the Mg-rich matrix.

Next, XPS was performed on the as-received material to compute the sub-surface material chemical composition of Mg, Li, and Al elements. In this study, we applied argon sputtering to remove ~ 20 nm of the material surface in order to reduce signal noise from the environmental contaminated surface. Figure 5 (a) shows the XPS full binding energy spectrum of the studied Mg-Li-Al alloy from a range of 560 to 0 eV. Characteristic peaks (i.e., O 1s, C 1s, and Mg$_{KLL}$) are labeled on the spectrum. In addition, the signature convoluted (Li 1s, Mg 2p) peak is also identified at ~ 50 eV. The C 1s peak is labeled at 284.8 eV, which indicates that the sample is fully charged and no peak shifting is needed. The insert on the left in Figure 5 (a) demonstrates a re-plotted spectrum extracted from the Thermo Scientific XPS library (XPS Interpretation of Magnesium), and the corresponding portion of the spectrum obtained in this study is boxed by red dotted lines. In this case, we observe an exact match between the two spectrum, indicating the existence of calcium (i.e., Ca 2s and Ca 2p$_{3/2}$ peaks) and oxide compounds in the current material. This is confirmed with EDS (not shown) where trace amounts of the Ca element on intact material surface are observed. However, no Ca is detected on the tested fragment surfaces post-experiment. Thus, we believe that calcium and the related CaCO$_3$ peak at ~ 550 eV comes from the outer environment, and the argon sputtering has not removed it completely.
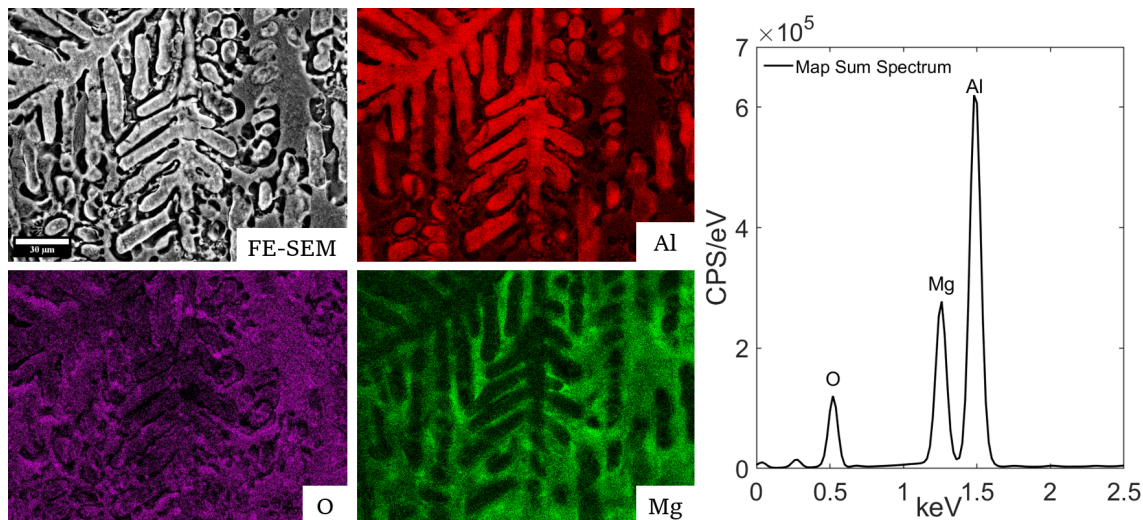
9

Figure 4: EDS mapping of the "fishbone" microstructure (see FE-SEM micrograph) showing high concentrations of the Al element, where these structures act as the "skeleton" of the material. A high concentration of Mg surrounds the Al-rich "skeleton" as the "matrix" (see Mg map). The O element distribution shows that the Mg-concentrated regions has a much higher oxidizing rate than the Al-concentrated regions (see O map). The map sum spectrum shown at the bottom right demonstrates the characteristic peaks for O, Mg, and Al elements. *The Li element as a light element cannot be analyzed using EDS.

Table 1: Sub-surface chemical composition of the studied Mg-Li-Al alloy computed by using X-ray photoelectron spectroscopy (XPS) method.

Element	Using Mg 2s, Al 2p, and Li 1s envelops (at%)	Converted to wt%	Using Al 2P, and the deconvoluted Li 1s and Mg 2p envelops (at%)	Converted to wt%
Mg	30.60	45.07	29.65	43.73
Li	48.22	34.64	48.44	35.87
Al	21.18	20.29	21.91	20.40

Figure 5 (b) - (d) show the high-resolution spectrum for the convoluted (Li 1s, Mg 2p), Al 2p, and Mg 2s peaks, respectively. These peaks are used to extract the relative atomic percentage of Mg, Li, and Al elements in the material. Component analysis is conducted on the convoluted peak (see Figure 5 (b)), where envelops are fitted to the individual peaks (green curve for Li 1s, red and purple curves for Mg 2p) using the Gaussian–Lorentzian (GL (30)) line shape. Two envelops (i.e., Mg 2s and the de-coupled Mg 2p) are used to obtain the sub-surface composition information. Table 1 shows the numerically integrated atomic percentages of Mg, Li, and Al elements using the high-resolution envelops, with conversion to weight percentage. From the table, it is observed that the two methods yield close results: (1) the Mg element of $\sim$ 30 at% (45 wt%), (2) the Li element of $\sim$ 48 at% (35 wt%), and (3) the Al element of $\sim$ 22 at% (20 wt%). The ternary phase diagram published by Goel et al. [59] and Dubost et al. [60] were compared with the

atomic percentage obtained in this investigation. With the corresponding atomic percentages of elements in the studied Mg-Li-Al, the phase diagram informs that the BCC β-Li and the LiAl phases should constitute the majority of the material phases, which is confirmed by our XRD analysis (see Figure 3). Furthermore, Goel and Cahoon [59] reported the reaction where a combination of HCP α-Mg, Li_2Mg, and Al_2LiMg was formed with 25 at% Al, 25 at% Li, and 50 at% Mg at room temperature of 419°C. It can be seen that with relatively high concentrations of Mg (in our case $\sim$ 30 at%), the current alloy retain a certain amount of $MgLiAl_2$ and Li_2Mg phases (see Figure 3).
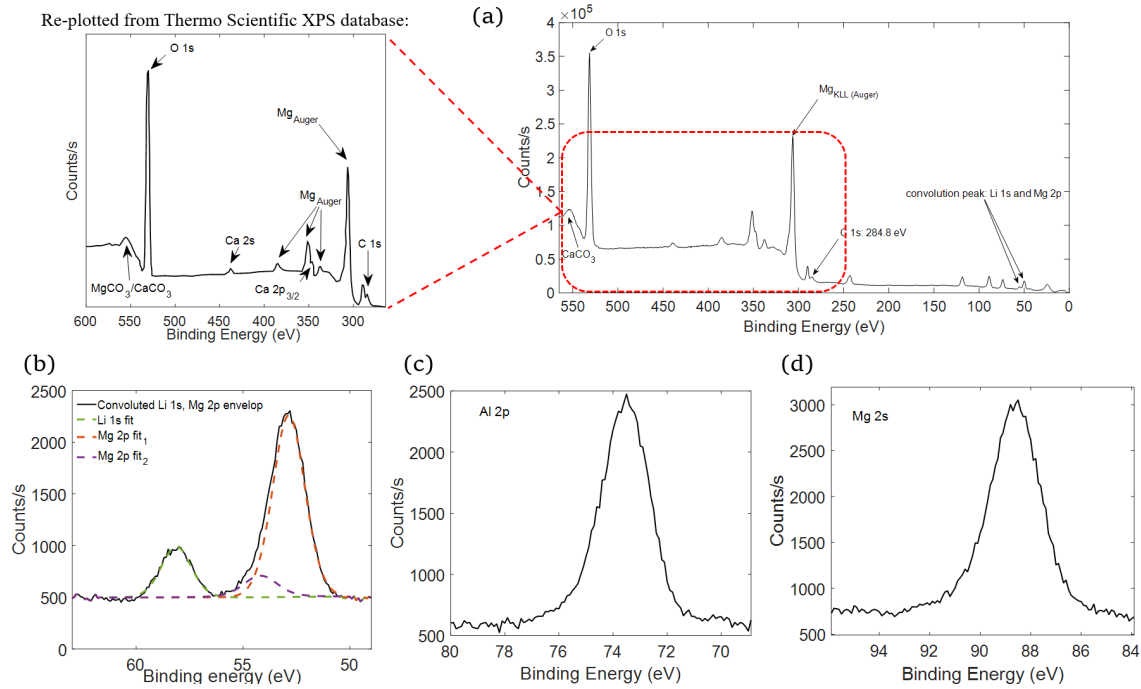

Figure 5: XPS investigation of the studied Mg-Li-Al alloy showing characteristic elemental peaks for chemical composition analysis. (a) Full spectrum showing the characteristic O 1s and C 1s peaks. The position of the C 1s peak at 284.8 eV shows that the sample is fully charged and peaks are at their correct positions. The insert on the left is extracted and replotted from Thermo Scientific XPS database (XPS Interpretation of Magnesium), which demonstrates an excellent match with the regions encompassed with red dotted lines. (b) High-resolution spectrum and the fitted envelop of convoluted Li 1s and Mg 2p peaks for composition calculations. (c) High-resolution envelop of Al 2p peak. (d) High-resolution envelop of Mg 2s peak.

3.2. Mechanical Property Assessment Using Micro-Hardness and Strain-Rate-Dependent Compression Experimentation

In this study, we assess the mechanical performance of the Mg-Li-Al alloy under compressive loading, including indentation micro-hardness and strain-rate-dependent uniaxial compression testing. While lower density is favorable to reduce energy usage, the capacity to bear compressive loading is essential in many structural applications (e.g., aerospace [61], defence [62], and automotive [63]), and we expect the studied

11

alloy to have high specific compressive strength and hardness, with reasonable ductility and malleability [8, 25, 33].

Shown in Figure 6 is the micro-hardness vs. density plot with comparisons to pure magnesium [64], some commercialized Mg-based alloys [64], and some recently developed Mg-Li-(Al_x) alloys [28, 32, 33, 65]. All hardness values measured in Vickers, Knoop, or Brinell methods are converted to GPa for the ease of comparison. The studied Mg-Li-Al alloy has a slightly lower density than the pure magnesium (~ 1.68 g/cm^3), while its micro-hardness is > 2x higher than all pure magnesium and commercialized Mg-based alloys. Here, we have found no anisotropy in micro-hardness on the PD and ND direction. Comparing with recently developed Mg-Li-Al_x alloys, it is observed that while adding Li can largely decrease the density of the materials (e.g., from ~ 1.72 to ~ 1.3 g/cm^3 with 15 wt% [33]), alloying with Al at a relatively high weight percentage could greatly enhance the micro-hardness (e.g., from ~ 0.45 GPa to ~ 1.25 GPa in a Mg-(11 wt%)Li-(0-3 wt%)Al alloy in [28]). This is attributed to the strengthening and nanoprecipitation effects from the Al addition [10, 28]. In the current study, the Mg-(35 wt%)Li-(20 wt%)Al alloy has a much higher concentration of both lithium and aluminum elements, and the trade-off between density and hardness seems to reach a good balance, with a superior micro-hardness (i.e., 1.63 ± 0.08 GPa) when compared with the other Mg-based alloys we reviewed (with most ≤ 1 GPa). To our best knowledge, some of the most recent developmental efforts towards the Mg-Li-(Al_x) alloys are made with lithium less than 20 wt% and aluminum less than 5 wt% [6, 17, 23, 31, 66]. The combination of elements in the current study is unconventional, and therefore, can yield a promising mechanical performance.

Next, we examine the mechanical response of the material through strain-rate-dependent uniaxial compression experiments. The representative compressive stress-strain curves across seven strain rates, from $\sim 10^{-5}$ to $\sim 10^3$ s^{-1} are shown in Figure 7. In general, the stress increases linearly up to ~ 0.005 strains, followed by a deviation from the constant slope. The gradient of the linear region is defined to be the Young's modulus of the studied Mg-Li-Al alloy. In this case, the Young's modulus across all strain rates is more-or-less constant and has an average of 66.2 ± 3.0 GPa, which is comparable to some of the aluminum alloys [67–69]. The Poisson's ratio, determined by averaging the slopes of the quasi-static lateral vs. axial strain curves taken at 0.005 strain, is found to be 0.24 ± 0.01 in the current material. From the stress-strain curves in Figure 7, continuous strain hardening occurs after the linear elastic region before reaching the peak stress, where we observe a higher strain hardening rate in all the dynamic curves compared to the quasi-static ones. This higher strain hardening rate under dynamic loading drives the peak stress to be reached earlier (i.e., at strains < 0.015). In this study, we define the peak stress to be the "compressive strength" of the material, and this will be investigated in detail in the subsequent figure (see Figure 8). After the peak stress is reached, the stress value of the quasi-static curves drops to zero with an end strain between 0.02 to 0.025, indicating a quasi-brittle material behavior with low fracture strain (defined as the strain at peak stress).
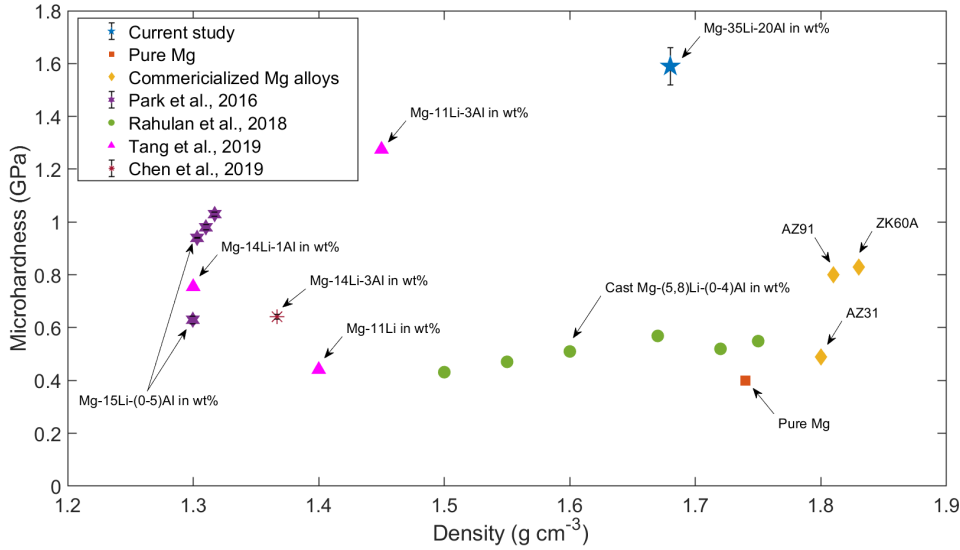
Figure 6: Micro-hardness evaluation of the studied Mg-Li-Al alloy, with comparison to pure Mg, commercialized Mg-based alloys, and similar Mg-Li-(Al_x) alloys recently developed in the literature [28, 32, 33, 65]. All hardness values are converted to GPa for the ease of comparison. Error bars are applied where applicable. The studied Mg-Li-Al shows a slightly smaller density than the pure Mg but superior hardness compared with all other alloys.

For the dynamic tests, we include the unloading part of the curves for completeness. The more gradual decrease in stress and strain is able to be captured because the ultra-high-speed imaging technique used in the SHPB setup can capture the failure process at higher frame rates.

Next, Figure 8 shows the compressive strength vs. strain rate in a semi-log scale to examine the strength rate-dependency in the studied Mg-Li-Al alloy. The horizontal error bar is associated with the uncertainties in determining the strain rates from the DIC strain-time history, and the vertical error bar accounts for the maximum uncertainty in sample dimensions (i.e., $\sim 2\%$). In this study, the material exhibits no significant strain-rate-dependency in strength across the strain rate regime we have investigated, with a nominal average compressive strength of 699.4 ± 74.0 MPa. The standard deviation is computed through error propagation analysis by considering the dimensional tolerances, showing the lower and upper bound of the strength. Of note, the strength of the studied alloy is $> 2x$ higher than most of the similar alloys reported in the literature, but with a much lower fracture strain (i.e., ~ 0.025 compared to > 0.1) [5, 8, 9, 28, 31, 38]. While most of the other Mg-Li-Al alloys in the literature demonstrate ductile behavior with a distinct yield point followed by a plastic regime, the alloy in this study shows a short linear elastic region followed by continuous strain hardening. We believe that the strain hardening and the insensitivity of the compressive strength are outcomes of the processing, constituent, microstructure, and failure mechanisms, which will be explored further in the Section 4.
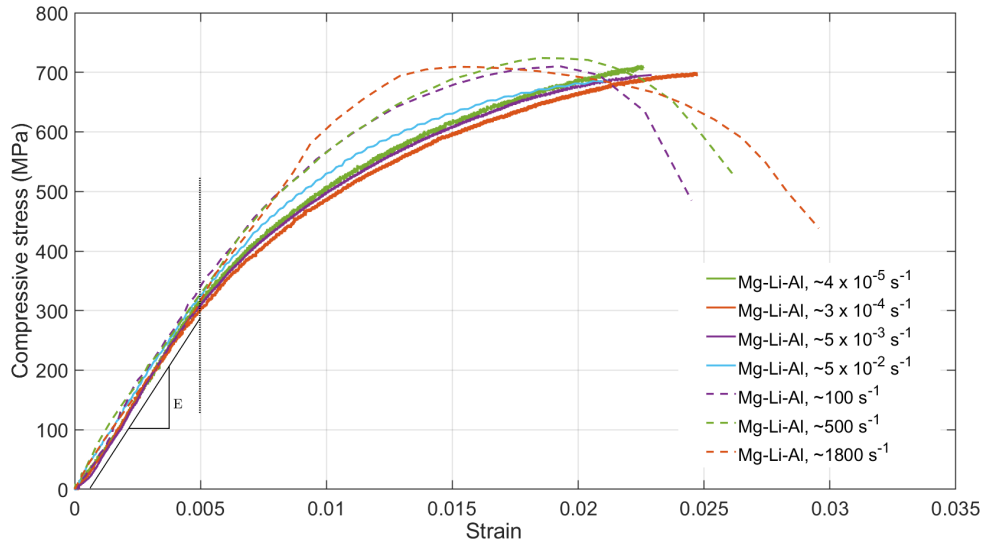
13

Figure 7: Representative stress-strain curves of the studied Mg-Li-Al under uniaxial compressive loading at different strain rates (from $\sim 10^{-5}$ to $\sim 10^3$ s^{-1}). All the quasi-static and dynamic stress-strain curves are obtained by matching the MTS and SHPB stress data with the DIC strain data in time, respectively. All quasi-static stress-strain curves are plotted with solid lines, whereas the dynamic ones are plotted in dashed lines. A vertical dotted line at 0.005 strain is marked to indicate where the Young's modulus and Poisson's ratio are extracted.
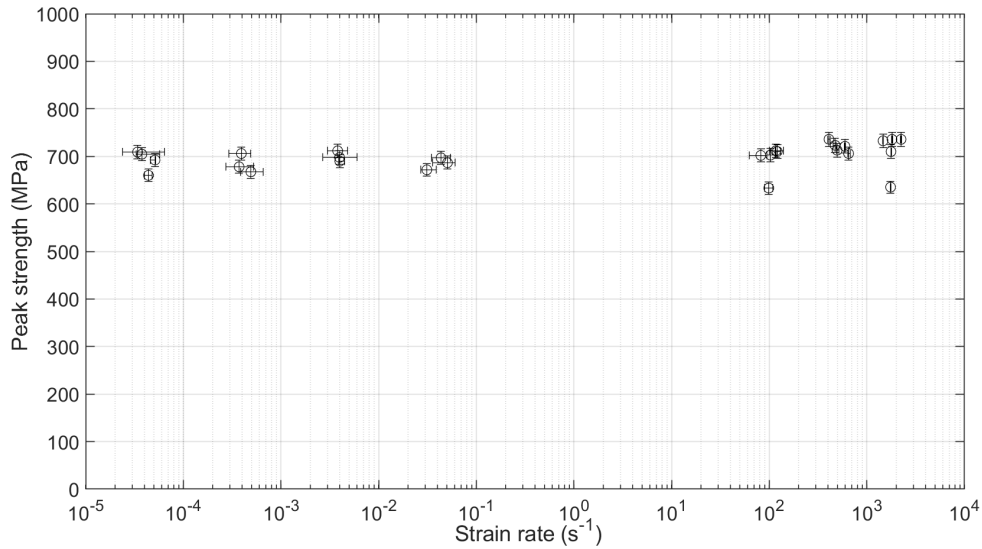

Figure 8: Peak strength of the studied Mg-Li-Al alloy plotted against strain rates in semi-log scale to visualize the strain-rate-dependency in strength from $\sim 10^{-5}$ to $\sim 10^3$ s^{-1}. No significant change in strength is observed across all strain rates. The horizontal error bar is obtained by taking the upper and lower limit of strain rate estimation from the DIC strain-time history, and the vertical error bar accounts for uncertainties in sample dimensions.

14

Finally, shown in Figure 9 are time-resolved high-speed images coupled with two dynamic stress-strain curves (i.e., curve colors matched with ones in Figure 7), with the frame number marked at the exact strain on the curves. T1-(1-4) and T2-(1-4) indicate the numbered frames extracted from test 1 and 2, respectively. Markers on the stress-strain curves are time-matched data points from stress-time and strain-time histories. Mapping the high-speed frames onto the unloading part of the stress-strain curves enables us to study the initiation and propagation of fracture and the time-resolved relationship with the stress-strain curves. In both sets of images, T1-(1,2) and T2-(1,2) correspond to the frames obtained at the start of the stress-strain curves and the peak stress, where no pre-fracture surface deformation features are observed (e.g., shear bands, twins, and texturing). The material does not buckle or undergo any significant change in geometry like common Mg and Al alloys [70], as it is quite brittle with fracture strains of < 0.025. The onset of fracture is seen (red arrows in Figure 9) at the end of the stress-strain curves (T1-3 and T2-3), and they are ~ 6 to 7 μs delaying from the peak stress. In both T1-3 and T2-3, the cracks initiate at the top and bottom edges of the sample at an angle of 30 to 45° from the loading direction, indicating a probable shear mode fracture. From T1-3 and T2-3, it is observed that only one or two primary cracks are initiated simultaneously at the onset of fracture. The DIC looses correlation after T1-3 and T2-3 because of the large surface discontinuity caused by fracture. Subsequently, T1-4 and T2-4 correspond to the frames where the correlation is lost (plotted on the x-axis) and the cracks propagate further. Shear fracture is the dominant failure mode in both Test 1 and 2, followed by crack bifurcation populated from the primary cracks. Consequently, it is evident that the current Mg-Li-Al alloy exhibits brittle fracture, which is notably different than the conventional Mg-based alloys where plastic deformations, such as twinning [71] and buckling [70], which occur before cracking.

3.3. Macroscopic Fracture Phenomenon and Crack Propagation Speed Measurements at Different Strain Rates

To better illustrate the surface fracture mode during loading and its relationship to the localized strain evolution, we map the DIC shear strain contours (ϵ_{xy}) on the high-speed still frames in Figure 10. Images are taken from a quasi-static experiment conducted at $\sim 10^{-3}$ s^{-1} (Figure 10 (a)) and a dynamic experiment carried out at ~ 1800 s^{-1} (Figure 10 (b)), with the corresponding axial strain values indicated in each frame. A shear strain spectrum bar ranging from -0.01 to 0.01 is labelled on the right to better visualize the features. In Figure 10 (a), the first image corresponds to the reference (undeformed) frame for the DIC analysis, where the green color indicates zero strain on the color bar. At ~ 0.001 axial strain, the global strain field is mostly homogeneous, with a slight variation in the shear strain ranging from 0.0005 to -0.0005. At approximately 0.016 axial strain, distinct localized shear strain fields are observed with two maximum positive fields located at the left edge of the sample. In addition, a negative shear strain zone spans the sample surface from the top right to bottom left, with several maximum negative localized fields occupying the area. In image 4 at ~ 0.025 axial strain, the shear strain-concentrated regions continues to grow into
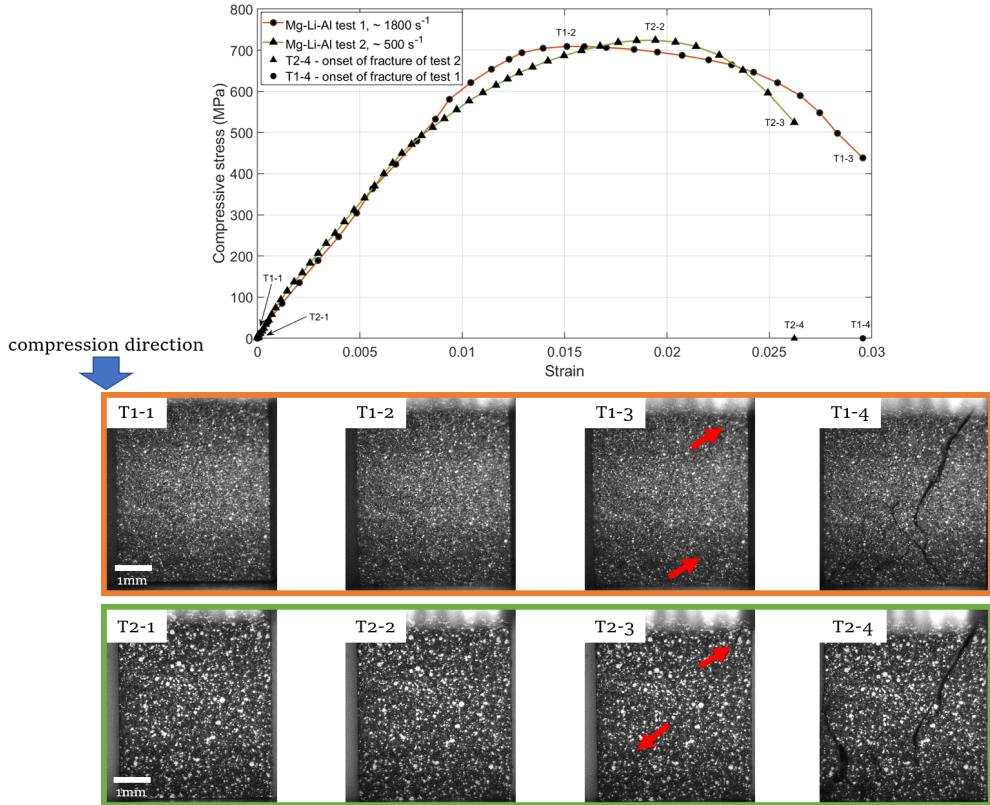
Figure 9: Time-resolved ultra-high-speed images coupled with two stress-strain curves obtained at ~ 500 and ~ 1800 s^{-1} strain rates, showing the strain associated with the onset of surface deformation. In both cases, cracks initiate at both the top and bottom of image 3 and propagate across the sample surfaces with a shear mode fracture. Image 3 corresponds to the last data point on the unloading part of the stress-strain curves, where both image 4 (T1-4 and T2-4 indicated on the x-axis) are taken right after the DIC correlation is lost, and they are indicated on the x-axis.

more positive or negative localized shear strain fields, with additional positive zones identified at the bottom right of the surface. At strains > 0.025, fracture is promoted through these regions, as indicated by the red arrows in image 5. Here, it is observed that all of the primary cracks initiate from maximum negative shear strain regions and propagate along the negative shear strain zone shown in image 3. Thus, shear-induced brittle fracture under quasi-static loading is believed to be the dominant fracture mode. Interestingly, the maximum positive shear strain fields appear to not facilitate in the crack initiation, but they do participate in promoting crack growth and coalescence.

Similar trends are observed in the dynamic experiments in Figure 10 (b) up to image 3 under dynamic loading, with the global shear strain field being homogeneous while localized fields start to develop. In image 3 at ~ 0.016 axial strain, while some maximum positive and negative shear fields are developed, no specific orientation of the shear zones are observed. In image 4 at ~ 0.025 axial strains, further growth of the shear strain does not reveal a clearer global shear zone either. This is in contrast to the quasi-static

16

experiments in Figure 10 (a) where the underlying shear mode fracture can be informed by the global shear
strain field. Furthermore, we pointed out the fracture sites by correlating the final crack pattern in image
5 (red arrows) to the absolute maximum shear strain field in image 4 of Figure 10 (b). In the dynamic
experiments, it appears that split cracks initiate from both the maximum positive and negative fields and
grow along these regions (e.g., maximum positive region in the middle of the top edge). Here, a mixture of
axial splitting and shear fracture is identified, with the splitting cracks propagating into the shear direction
and eventually causing ultimate failure. We believe the additional micro-cleavage mechanism activated under
dynamic loading drive the mix-mode fracture phenomenon, and this will be examined in Section 3.4.
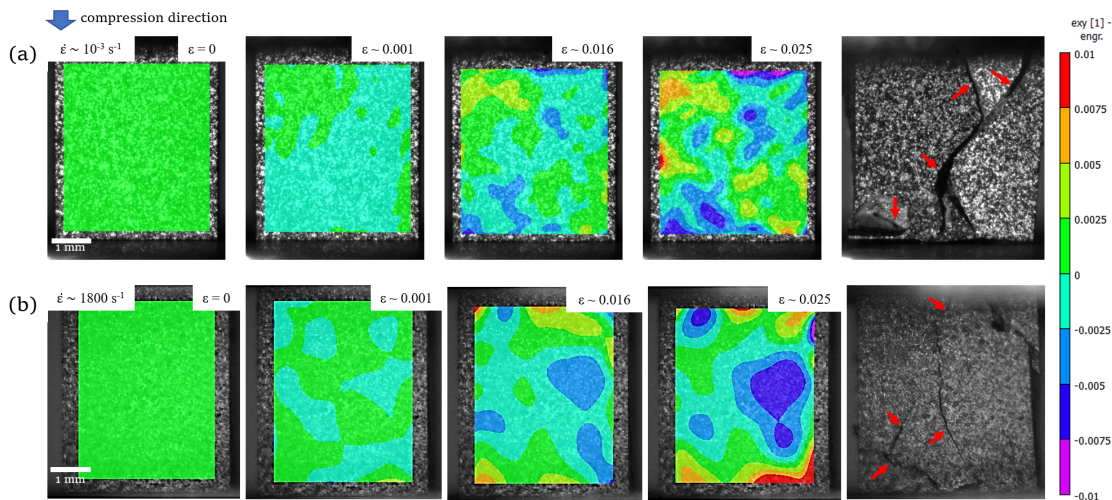

Figure 10: DIC shear strain contour (ϵ_{xy}) overlapped with high-speed still frames showing shear strain evolution associated with
the onset of fracture. Axial strain value is label on the top right corner of each sub-figure. Red arrows indicate the dominant
cracks that lead to ultimate failure. (a) Testing at a strain rate of $\sim 10^{-3}$ s^{-1}. (b) Testing at a strain rate of ~ 1800 s^{-1}.

Lastly, the crack propagation speed is estimated in all dynamic tests and plotted against strain rate in
Figure 11. Note that we are only able to measure the crack propagation speeds during dynamic testing
because of the limited camera frame rate in quasi-static experiments. In each test, the mean crack propa-
gation speed is estimated by averaging over the first two dominant surface cracks, and the individual crack
propagation speed is computed through consistently tracking the crack tip and dividing the apparent crack
length (i.e., measured from the origin of the crack to the crack tip) by the propagation time (i.e., how many
frames are taken to grow from zero to the apparent crack tip). A similar approach has been used by Kannan
et al. [72] on Mg-based alloy to measure twin growth velocities. Uncertainties in measurements come from
the dimensional tolerance, crack length measurements (i.e., ~ 3 pixels on each side equate to $\sim 6\%$ in error),
and human error in selecting the frames resulting in time increment differences (i.e., ~ 1 frame). The total
error of each measurement could be as large as $\sim 25\%$. To reduce the scattering in measurements, we use
the median value of the five repeated measurements taken for every single crack. In Figure 11, three regions

17

of speeds are observed which are correlated to the three different strain rates we access in dynamic testing, and a positive correlation between speed and strain rate is identified with $R^2 = 0.95$. The crack propagation speed is low in the studied alloy ranging from ~ 480 m/s at ~ 100 s^{-1} to ~ 1000 m/s at ~ 2000 s^{-1}. These values are low when compared to other brittle solids tested under compression-type loading at high strain rates (e.g., SHPB, edge-on-impact, shock), such as advanced ceramics and glasses where the reported crack propagation speeds are usually in the range of thousands to over ten thousand meters per second [73, 74]. In general, we believe the cracking in this material is related to the dendritic "fishbone" microstructure and the associated "peeling" failure mechanisms, which will be explored next in Section 3.4.
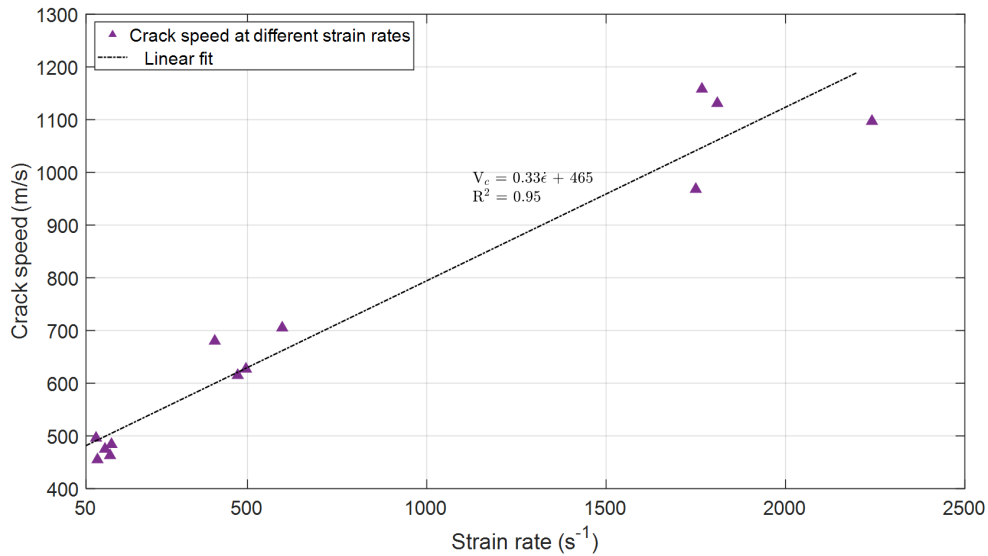

Figure 11: Crack propagation speed is plotted against strain rate demonstrating a positive correlation. The crack propagation speed is estimated from the high-speed images, and only dynamic tests are considered. The determination of the crack propagation speed can result up to 25% in total errors. *Note that these are only an approximation based on the conditions and assumptions we make in their measurements.

3.4. Fractography

In this section, we identify three dominant mechanisms that facilitate failure, termed "peeling" [75, 76] and "micro-cleavage" [77, 78]. These failure mechanisms are believed to be associated with the brittle nature of the studied Mg-Li-Al alloy (see Figure 9), strain rate insensitivity of the peak strength (see Figure 8), changes in the strain hardening rate (see Figure 7), and the macroscopic fracturing modes. As will be shown, peeling is mainly found in the Al-rich phases across all the investigated strain rates in this study, while micro-cleavage is an additional mechanism found in Mg-rich phases under dynamic loading.

Shown in Figure 12 are the micrographs taken from a test conducted at a quasi-static loading rate of $\sim$ 5 x 10^{-5} s^{-1}, with EDS maps confirming the elemental composition of the fracture sites. In Figure 12 (a),

18

a hilly "fishbone" microstructure is identified in the middle of the image, with the surrounding materials consistently lower in altitude. This happens when the top layer of the material is "peeled" away from the fracture plane, with the "fishbone" structure acting as the prevailing failure plane. In addition, a high density of micro-cracks is observed on the "fishbone" branches and grows perpendicular to the mainframe of the structure. High concentrations of aluminum on the "fishbone" is confirmed by the Al map, and the surrounding materials are magnesium-rich (see Mg map). Figure 12 (b) shows an opposite effect of the peeling mechanism, where a crater of the "fishbone" is left on the fracture surface after the top material layer has been removed. Both Al and Mg maps demonstrate clear layouts of the "fishbone" crater, with high concentrations of Al filling in the mainframe and branches, and the Mg clustered in the surrounding areas. Dense micro-cracks are also seen on the branches. Surrounding the damaged "fishbone" crater, minimal fracture is observed in the magnesium-rich matrix, and the fracture sites are smeared, indicating ductile rupture and potential localized melting [65, 79]. This suggests that the Al-rich "fishbones" are brittle in nature, which results in cracking-dominant failure. On the other hand, the Mg-rich matrix is more ductile and likely does not govern the macroscopic fracture mode in this material. In conclusion from Figure 12, we believe that peeling is the dominant failure mechanism of the studied Mg-Li-Al alloy under quasi-static loading. Given the growth orientation of the "fishbone" structure, it is also likely that long shear-type cracks will initiate and develop at locations of high stress concentrations (i.e., similar to mode II fracture [80]) while the material is peeled away along the mainframe, yielding macroscopic fractures with a distinct shear zone (see Figure 10 (a)).

For dynamic testing, globally distributed micro-cracks and micro-cleavages are observed in both Al and Mg-rich regions on the fracture planes (see Figure 13 (a)). The micro-cleavage is a newly observed failure mechanism at these strain rates, which is likely a consequence of the high kinetic energy and inertia force generated in a short time period during high rate compression. Furthermore, micro-cleavages tend to accumulate in the Mg-concentrated regions (see Mg map), indicating new pathways for crack growth and coalescence, and therefore, a plausible way of energy dissipation. In addition, at least two "fishbone" craters are identified in the micrograph (red arrows). The magnified view on a single "fishbone" crater in Figure 13 (b) confirms this observation, with complete absence of the Mg element on the skeleton. This observation of the "fishbone" craters on a highly damaged fracture plane demonstrates peeling as a universal failure mechanism across all strain rates studied here (i.e., between $\sim 10^{-5}$ and $\sim 10^{3}$ s^{-1}). The activation of micro-cleavages from the softer and weaker Mg-rich regions under high-rate loading is similar to the argument made in brittle materials, where cracks tend to initiate and propagate concurrently from a network of defects/flaws under dynamic loading, resulting in macroscopic splitting and smaller fragments [81–83]. For the current Mg-Li-Al alloy, we observe split-cracking behavior under dynamic loading (see Figure 10 (b)) with much smaller fragments, and this results in a mixed-mode fracture when peeling is taken into account
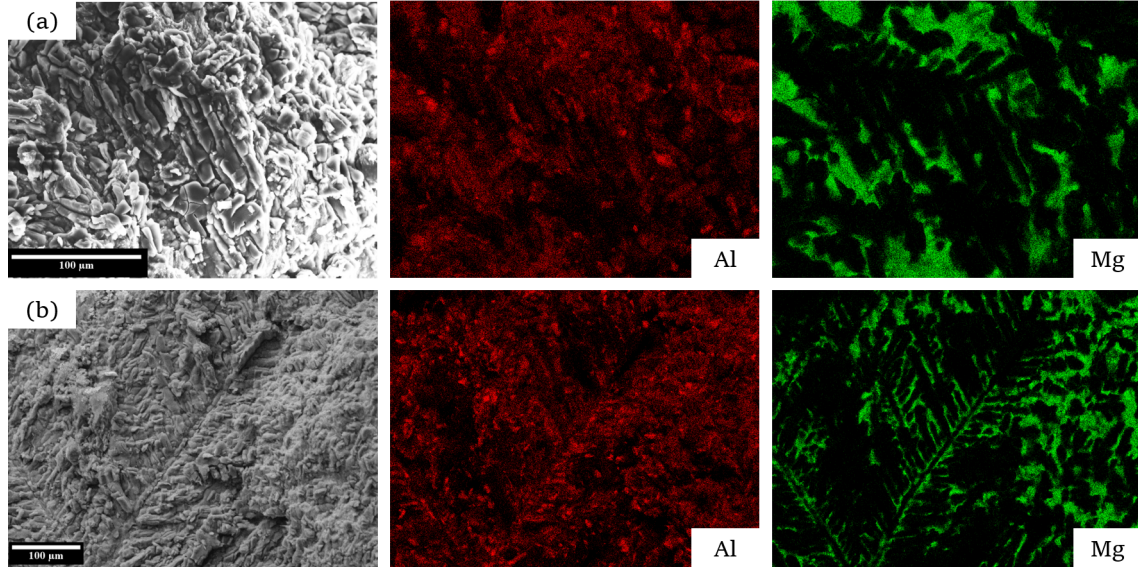
Figure 12: Post-mortem SEM micrographs showing failure mechanisms of the studied Mg-Li-Al alloy tested at a strain rate of $\sim 5 \times 10^{-5}$ s^{-1}. (a) A hilly "fishbone" structure demonstrating a layer of material that is "peeled" from the fracture plane. The Al map confirms the high-concentration of aluminum for the "fishbone" structure, and the Mg map shows that magnesium only appears in the surrounding areas. Dense micro-cracking is observed on the "fishbone" branches. (b) An opposite effect of the peeling mechanism revealing a crater is left behind after the "fishbone" structure is removed from the fracture plane. Overlapping of the Al and Mg maps confirm elemental composition of the "fishbone" crater.

(i.e., no distinct shear zone is observed).

4. Discussion

In this section, we seek to expand and provide new explanations for better understanding the mechanical behavior of the studied Mg-Li-Al alloy. In Sub-section 4.1, the strain rate insensitivity of the peak strength and change in strain hardening rate prior to peak strength will be explored in the context of constituents, microstructure, and failure mechanisms. Insights from the literature will be provided regarding the unique composition, microstructure, and mechanical properties of the studied Mg-Li-Al alloy. Next in Sub-section 4.2, previous studies on (quasi-)brittle solids will be surveyed with the focus on crack/damage propagation speed under compressive loading, and this will provide some ideas into the mechanical response of the current Mg-Li-Al material. Finally, the importance of accounting for crack growth rates in models will be outlined.

4.1. Microstructure-Associated Mechanical Performance of the Studied Mg-Li-Al Alloy

4.1.1. The Strain Rate Insensitivity of the Peak Strength

In this study, we performed strain-rate-dependent uniaxial compression experiments on the Mg-(~ 35 wt%)Li-(~ 20 wt%)Al alloy from $\sim 10^{-5}$ to $\sim 10^{3}$ s^{-1} strain rate and found the peak strength with an average
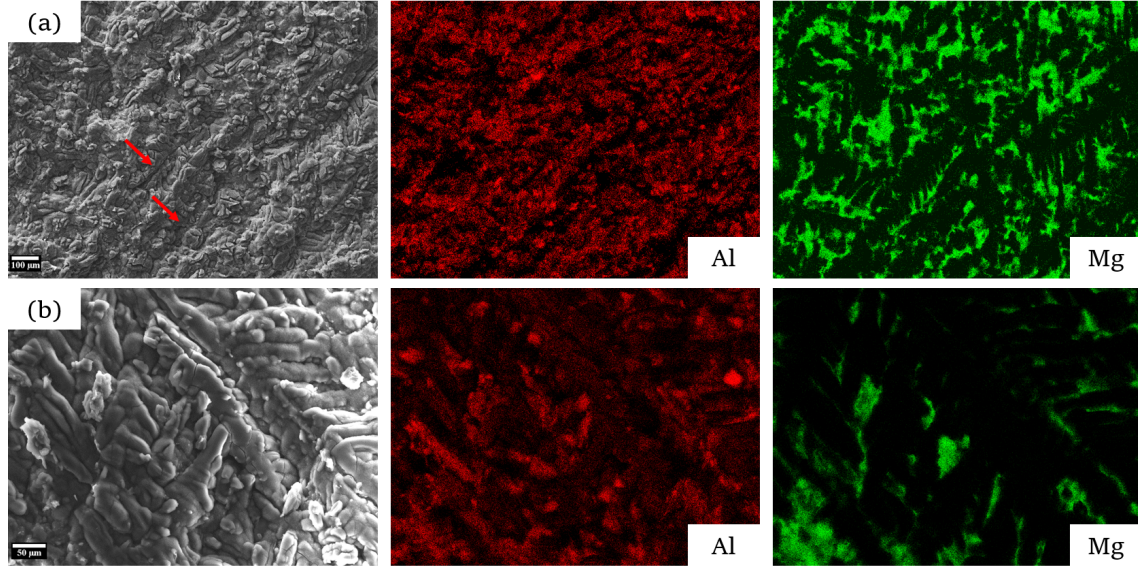
20

Figure 13: (a) SEM micrographs showing failure mechanisms of the studied Mg-Li-Al alloy tested at ~ 1800 s^{-1}. Extensive amounts of micro-cleavages are accumulating in the Mg-rich regions. "Fishbone" craters are observed at the bottom of the micrograph (red arrows), which are verified by the absence of magnesium in the corresponding regions in the Mg map. (b) Magnified view on the fishbone crater showing branching fracturing. This confirms existence of peeling as a universal failure mechanism under the investigated strain rates (10^{-5} to 10^3 s^{-1}).

of 699.4 ± 74.0 MPa. To our best knowledge, very limited studies focused on the strain-rate-dependency of the Mg-Li-Al materials [39, 84]. For example, Guo et al. [39] investigated the strain rate effect on a Mg-(8 wt%)Li-(1 wt%)Al-(1 wt%)Ce alloy from 10^{-4} to 2700 s^{-1}. They found an increase in flow stress (taken at 0.16 strain) from ~ 275 MPa at 0.0001 s^{-1} to ~ 425 MPa at 2000 s^{-1}. The strain rate effect on the flow stress was attributed to the change in the deformation mechanism from thermal activation of dislocations under quasi-static conditions to twinning-dominant under dynamic conditions. However, no strain-rate-dependency is observed in this study for the current alloy. We believe that two factors may contribute to this outcome, detailed subsequently:

First, past studies have shown that brittle materials exhibit less strain-rate-dependency under compression when compared to ductile materials [45, 85–89]. This is because brittle materials usually fail as a consequence of cracking-dominant mechanisms (below the Hugoniot Elastic Limit) before a stress level is reached to induce plasticity [89]. We observe similar phenomenon in the current material (see Figure 9 and Figure 10). For ductile materials, additional plastic deformation mechanisms can be activated with increases in loading rates (e.g., twinning [39, 90, 91], (dislocation) slipping [92, 93], and dynamic recrystalization [94, 95]). The activation or increase in areal density of these plastic deformation mechanisms promote further stress build-up in the materials before fracture, and contribute to their strain-rate-dependent response. None of these plastic deformation mechanisms are either observed or dominant in the current material.

21

Second, the architectured "fishbone" microstructure of the studied material may also contribute to the strain rate insensitivity in strength. Past studies on additive manufactured materials involving structured materials (e.g., 3D-printed materials) showed very different rate sensitivities in strength [96–100]. For example, Zhang et al. [96] found an ~ 3.6x increase in yield strength (from ~ 70 MPa at 0.001 s^{-1} to ~ 250 MPa at 1 s^{-1} at 1193 K) for a TiBw/TA15 composite with a honeycomb TiB network. In another study, Ponnusamy et al. [97] found nearly no change in the flow stress between 0.01 s^{-1} and 700 s^{-1} strain rate for a selective laser melted AlSi12 alloy. In the studied Mg-Li-Al alloy here, the "fishbone" structure is the primary initiation site for failure at all strain rates we investigated (from $\sim 10^{-5}$ to 10^3 s^{-1}) (see Figure 12 and 13). Given that the stress concentration could easily occur at such structures with low aspect ratio (i.e., with pointy skeletons) and result in fracture, we believe that this is likely a factor contributing to the strain rate insensitivity in strength.

4.1.2. Changes in the Strain Hardening Rate from Quasi-Static to Dynamic Loading

In this study, stress-strain curves of the current Mg-(~ 35 wt%)Li-(~ 20 wt%)Al alloy at different strain rates were obtained, and these showed an increase in strain hardening rate under dynamic loading (see Figure 7). The change in strain hardening rate is likely an outcome of the competition between dislocation strain hardening and flow softening caused by the newly activated micro-cleavage mechanism under dynamic loading (see Figure 13) [8, 31, 38, 101, 102]. Furthermore, we believe the changes in the strain hardening rate is mainly associated with the Mg-rich matrix since the Al-rich "fishbone" structures dictate the brittle fracture process, and the "fishbone" peeling appears in all investigated strain rates. For example, Bi et al. [101] and Zhu et al. [102] explained in their works for an AZ31 Mg and a Mg-(7 wt%)Sn-(5 wt%)Zn-(3 wt%)Al alloys that the formation of micro-cracks was the major contributor to flow softening by consuming strain energy. In another study, Islam et al. [31] denoted an increase in strain hardening on a Mg-(14 wt%)Li-(1 wt%)Al alloy caused by multiplication of entrapped dislocations with increasing strain rates. Another study by Zou et al. [8] reported a similar compressive stress-strain behavior without a distinct yield point for a Mg-(3 wt%)Li-(6 wt%)Al alloy. They attributed this behavior to the dislocation-governed strain hardening process overcoming the dynamic recovery softening. In the current Mg-Li-Al alloy under dynamic loading, it appears that the greater dislocation strain hardening dominates prior to the peak strength resulting in a higher hardening rate, then the activation of micro-cleavages causes flow softening resulting in the gradual decrease of the stress-strain curves (see Figure 9).

4.2. Crack Propagation Speed and its Modelling Perspectives

In this Sub-section, we outline two crack characteristics of the studied Mg-Li-Al alloy: the microstructure-associated strain-rate-dependent mode of brittle fracture and the crack propagation speed. While the mode of fracture as an important input in modelling damage are well explored [103–106], crack propagation speed

22

(i.e., crack propagation velocity, damage front velocity, or fracture velocity) is still not widely studied for brittle solids [107–109]. In the second part of this Sub-section, we will compare the crack propagation speed of the current alloy to the ones reported in the literature for different quasi-brittle and brittle materials (e.g., concrete, rock, ceramics). The importance of accounting for crack propagation speeds in models will also be briefly discussed.

First, in the current Mg-($\sim$ 35 wt%)Li-($\sim$ 20 wt%)Al alloy, the "fishbone" microstructure is believed to be the major site for fracture initiation in both quasi-static and dynamic experiments. Under compressive loading, the associated peeling mechanism of the "fishbone" (see Figure 12 and Figure 13) is similar to the mode II fracture [110], where the shear stress is usually considered as the critical stress to promote failure. This dendrite microstructure of the current material results in shear mode cracking observed on the sample surface (see Figure 9). DIC ϵ_{xy} contours in Figure 10 confirms the mode of fracture, where cracks grow along the maximum and minimum shear localized regions. In contrast to the quasi-static experiment where the crack propagates in a diagonal shear zone (see Figure 10 (a)), the dynamic experiments show more spatially distributed localized shear strain regions. These localized regions promote a mix mode of split and shear cracking under dynamic loading (see Figure 10 (b)), which is not observed under quasi-static conditions. The splitting cracks appear to be the consequence of initiation, growth, and coalescence of the micro-cleavages under dynamic loading (see Figure 13). The formation of splitting cracks from a large number of micro-cleavages could be analogous to the nucleation of columnar cracks in brittle materials under dynamic loading (e.g., ceramics) [81, 111, 112]. Eventually, the splitting cracks merge into the larger shear cracks and result in failure, indicating shear mode fracture is dominant in the current material.

Second, we measure the crack propagation speed of the current material using ultra-high-speed frames and found an increasing trend from $\sim$ 480 m/s at $\sim$ 100 s^{-1} to $\sim$ 1000 m/s at $\sim$ 2000 s^{-1}. Crack propagation speed measurements are limited in the literature, and some of the early studies were reported mainly in rocks and concretes [106, 107, 113, 114]. In those materials, the crack propagation velocities were reported as $\sim$ 170 m/s for a sandstone under dynamic compression [115], and between 63.4 and 681.7 m/s for a granite from quasi-static to dynamic loading [107]. A review by Zhang and Zhao [113] documented a large span of crack propagation speeds ranging from 10^1 to 10^4 m/s for rock-like materials. The large differences could come from the measuring techniques, types of materials, loading rates, and stress states. From a modelling perspective, the elastic energy at the crack tip and the dynamic propagating toughness will affect the crack propagation speed [116]. Attentions for crack propagation speed measurements have been extended to advanced ceramics and brittle metal matrix composites [73, 74, 117–119]. For example, Strassburger et al. [74, 117, 118] reported the damage velocity (i.e., velocity of the fastest fracture) for several types of ceramics and cermets using edge-on-impact experiments. The damage velocity ranged from $\sim$ 2500 to $\sim$ 5500 m/s for WC and from $\sim$ 4800 to $\sim$ 11000 m/s for SiC-B at impact velocities from 100 to 1000 m/s. In addition,

23

the damage velocities seemed to increase much slower after a certain transitional impact velocity, and they all approach the longitudinal wave speed at sufficiently high impact velocities [118].

The crack propagation speed of the current Mg-Li-Al alloy seems to be generally higher than quasi-brittle solids such as rocks, but it is much lower than that in linear elastic materials like ceramics. Sha et al. [120] reported a maximum crack propagation speed of ~ 1250 m/s for Mg-(3.3 wt%)Li and ~ 935 m/s for Mg-(14 wt%)Li alloys in SHPB experiments, which agrees reasonably with our measurements of ~ 1000 m/s at ~ 1800 s^{-1}. The decrease in crack propagation speed between their two alloys in [120] was attributed to the change from a brittle to ductile fracture mode because of the increase in Li content (i.e., HCP to BCC phase transformation). In the material under investigation in this current paper, the dendritic "fishbone" structure is likely the controlling factor of crack initiation and propagation (see Figure 2 and 12). It is worth noting that past studies rarely reported the associated strain rates with the crack propagation speeds. We see in our study that there is a positive correlation between crack propagation speed and strain rate at least in the strain rate regime we investigated (see Figure 11). A full strain rate spectrum study including the quasi-static condition (i.e., with ultra-high-speed imaging) and the shock condition (i.e., plate impact or laser shock experiments) is desired [45, 121, 122].

Lastly, different modelling approaches have been employed recently to extract crack propagation speed information during simulations, including tensile crack softening failure criterion [48], effective strain-rate-dependent non-local damage modelling [109], peridynamic modelling [123], linear complete extended finite element method (XFEM) [124], and variational phase-field modelling [125]. In general, efforts in advanced modelling of damage aim at solving the time-resolved evolution of properties and mechanisms, including crack growth characteristics [126–128]. The ability to determine crack propagation speed is important to sub-micron structural responses, such as fragmentation under impact loading [129–131]. The accuracy in capturing crack propagation speeds are associated with, for example, stress wave speeds (e.g., longitudinal, Rayleigh) [123], mixed-mode fracture energies [125], and the damage gradient [132]. Overall, crack propagation speed measurements provide an important parameter for model validation, given the fast-evolving micro- and meso-scale models used to simulate damage growth in brittle materials [133–136]. Therefore, more attention on quantifying crack characteristics utilizing advanced high-speed imaging or other in-situ measuring techniques should be considered in the materials research community.

5. Conclusion

This study assessed the mechanical performance of a Mg-(~ 35 wt%)Li-(~ 20 wt%)Al alloy through detailed characterization, micro-hardness testing, and strain-rate-dependent uniaxial compression experiments. The Al-rich "fishbone" structure was observed as a result of the unique combination of high Li and Al weight percentages. Micro-hardness of the studied material was measured as 1.63 ± 0.08 GPa at a density of $\sim$

1.68 g/cm^3, and the micro-hardness is the highest among all surveyed Mg-Li-Al$_x$ alloys. The stress-strain response under strain-rate-dependent uniaxial compression showed continuous strain hardening followed a small linear elastic region, with a peak strength of 699.4 $\pm$ 74.0 MPa. The high specific strength and hardness make the current Mg-Li-Al alloy attrative for aerospace and transportation applications. High-speed images coupled with DIC studies showed that shear mode fracture was the dominant failure mechanism in the material, while an additional splitting crack mechanism was observed under dynamic loading. In addition, crack propagation speed measurements were reported for the studied Mg-Li-Al alloy as $\sim$ 480 m/s at $\sim$ 100 s^{-1} to $\sim$ 1000 m/s at $\sim$ 2000 s^{-1}. Lastly, post-mortem SEM investigation demonstrated that "fishbone" peeling was the main contributor to shear fracture at all strain rates, and the activation of micro-cleavage was determined in the Mg-rich matrix only under dynamic loading. Linking mechanical properties and the associated strain-rate-sensitivity to microstructure-promoted fracture mechanisms and their characteristics is essential in understanding the material performance.

6. Acknowledgment

7. Data Availability

The raw/processed data related to this study can be shared per request to the corresponding author (Haoyang Li) at haoyang@ualberta.ca.

References

[1] Z. Liu, K. Zhang, X. Zeng, Theoretical basis and application of magnesium-base lightweight alloys (2002).

[2] M. Zhang, F. Elkin, Magnesium–lithium superlight alloys (2010).

[3] C. Li, D. Xu, X.-B. Chen, B. Wang, R. Wu, E. Han, N. Birbilis, Composition and microstructure dependent corrosion behaviour of mg-li alloys, Electrochimica Acta 260 (2018) 55–64.

[4] B. Jiang, D. Zhang, J. Peng, P. Ding, Application and investigation of mg-li alloys, Materials Review 19 (5) (2005) 38–41.

[5] Y.-h. Sun, R.-c. Wang, C.-q. Peng, F. Yan, Y. Ming, Recent progress in mg-li matrix composites, Transactions of Nonferrous Metals Society of China 29 (1) (2019) 1–14.

[6] B.-J. Wang, J.-Y. Luan, D.-K. Xu, J. Sun, C.-Q. Li, E.-H. Han, Research progress on the corrosion behavior of magnesium–lithium-based alloys: A review, Acta Metallurgica Sinica (English Letters) 32 (1) (2019) 1–9.

[7] R. Wu, Z. Qu, M. Zhang, Reviews on the influences of alloying elements on the microstructure and mechanical properties of mg–li base alloys, Rev. Adv. Mater. Sci 24 (3) (2010) 35–43.

[8] Y. Zou, L. Zhang, Y. Li, H. Wang, J. Liu, P. K. Liaw, H. Bei, Z. Zhang, Improvement of mechanical behaviors of a superlight mg-li base alloy by duplex phases and fine precipitates, Journal of Alloys and Compounds 735 (2018) 2625–2633.

[9] J. Jackson, P. Frost, A. C. Loonam, L. Eastwood, C. Lorig, Magnesium-lithium base alloys—preparation, fabrication, and general characteristics, JOM 1 (2) (1949) 149–168.

[10] L. Wu, C. Cui, R. Wu, J. Li, H. Zhan, M. Zhang, Effects of ce-rich re additions and heat treatment on the microstructure and tensile properties of mg–li–al–zn-based alloy, Materials Science and Engineering: A 528 (4-5) (2011) 2174–2179.

[11] H. Zhong, L. Feng, P. Liu, T. Zhou, Design of a mg-li-al-zn alloy by means of calphad approach, Journal of computer-aided materials design 10 (3) (2005) 191–199.

[12] R. S. Busk, D. L. Leman, J. J. Casey, The properties of some magnesium-lithium alloys containing aluminum and zinc, JOM 2 (7) (1950) 945–951.

[13] T. Liu, S. Wu, S. Li, P. Li, Microstructure evolution of mg–14% li–1% al alloy during the process of equal channel angular pressing, Materials Science and Engineering: A 460 (2007) 499–503.

26

[14] C.-C. Hsu, J.-Y. Wang, S. Lee, Room temperature aging characteristic of mglialzn alloy, Materials transactions 49 (11) (2008) 2728–2731.

[15] S. Kamado, Y. Kojima, Deformability and strengthening of superlight mg-li alloys, Metallurgical Science and Tecnology 16 (1) (1998).

[16] F. Cao, H. Ding, Y. Li, G. Zhou, J. Cui, Superplasticity, dynamic grain growth and deformation mechanism in ultra-light two-phase magnesium–lithium alloys, Materials Science and Engineering: A 527 (9) (2010) 2335–2341.

[17] Y. He, C. Peng, Y. Feng, R. Wang, J. Zhong, Effects of alloying elements on the microstructure and corrosion behavior of mg–li–al–y alloys, Journal of Alloys and Compounds (2020) 154344.

[18] P. Fei, Z. Qu, R. Wu, Microstructure and hardness of mg–9li–6al–xla (x= 0, 2, 5) alloys during solid solution treatment, Materials Science and Engineering: A 625 (2015) 169–176.

[19] Y. Sun, R. Wang, J. Ren, C. Peng, Z. Cai, Microstructure, texture, and mechanical properties of as-extruded mg-xli-3al-2zn-0.2 zr alloys (x= 5, 7, 8, 9, 11 wt%), Materials Science and Engineering: A 755 (2019) 201–210.

[20] Y.-H. Kim, J.-H. Kim, H.-S. Yu, J.-W. Choi, H.-T. Son, Microstructure and mechanical properties of mg–xli–3al–1sn–0.4 mn alloys (x= 5, 8 and 11 wt%), Journal of alloys and compounds 583 (2014) 15–20.

[21] G. Grube, H. Zeppelin, H. Bumm, Elektrische leitfähigkeit und zustandsdiagramm bei binären legierungen. 11. mitteilung. das system lithium-magnesium, Zeitschrift für Elektrochemie und angewandte physikalische Chemie 40 (3) (1934) 160–164.

[22] A. Nayeb-Hashemi, J. Clark, A. Pelton, The li-mg (lithium-magnesium) system, Bulletin of alloy phase diagrams 5 (4) (1984) 365–374.

[23] Y. Li, T. Li, Q. Wang, Y. Zou, Effects of li on microstructures and corrosion behaviors of mg–li–al alloys, in: Magnesium Technology 2019, Springer, 2019, pp. 127–134.

[24] J. Dutkiewicz, P. Bobrowski, S. Rusz, O. Hilser, T. A. Tański, W. Borek, M. Łagoda, P. Ostachowski, P. Pałka, G. Boczkal, et al., Effect of various spd techniques on structure and superplastic deformation of two phase mglial alloy, Metals and Materials International 24 (5) (2018) 1077–1089.

[25] W. Xu, N. Birbilis, G. Sha, Y. Wang, J. E. Daniels, Y. Xiao, M. Ferry, A high-specific-strength and corrosion-resistant magnesium alloy, Nature materials 14 (12) (2015) 1229–1235.

[26] V. Kumar, K. Philippe, R. Shekhar, K. Balani, et al., Processing and nano-mechanical characterization of mg-li-al based alloys, Procedia Materials Science 5 (2014) 585–591.

[27] J. Wu, D. Zhao, J. M. Ohodnicki, B. Lee, A. Roy, R. Yao, S. Chen, Z. Dong, W. R. Heineman, P. N. Kumta, In vitro and in vivo evaluation of multiphase ultrahigh ductility mg–li–zn alloys for cardiovascular stent application, ACS Biomaterials Science & Engineering 4 (3) (2017) 919–932.

[28] S. Tang, T. Xin, W. Xu, D. Miskovic, G. Sha, Z. Quadir, S. Ringer, K. Nomoto, N. Birbilis, M. Ferry, Precipitation strengthening in an ultralight magnesium alloy, Nature communications 10 (1) (2019) 1–8.

[29] M. Krol, Effect of grain refinements on the microstructure and thermal behaviour of mg–li–al alloy, Journal of Thermal Analysis and Calorimetry 133 (1) (2018) 237–246.

[30] M. Furui, C. Xu, T. Aida, M. Inoue, H. Anada, T. G. Langdon, Improving the superplastic properties of a two-phase mg–8% li alloy through processing by ecap, Materials Science and Engineering: A 410 (2005) 439–442.

[31] R. Islam, A. Hadadzadeh, M. Wells, M. Haghshenas, Thermomechanical processing of an ultralight mg-14li-1al alloy, The International Journal of Advanced Manufacturing Technology 110 (11) (2020) 3221–3239.

[32] N. Rahulan, S. Gopalan, S. Kumaran, Mechanical behavior of mg-li-al alloys, Materials Today: Proceedings 5 (9) (2018) 17935–17943.

[33] G. H. Park, J. T. Kim, H. J. Park, Y. S. Kim, H. J. Jeong, N. Lee, Y. Seo, J.-Y. Suh, H.-T. Son, W.-M. Wang, et al., Development of lightweight mglial alloys with high specific strength, Journal of Alloys and Compounds 680 (2016) 116–120.

[34] H.-C. Chen, F.-Y. Hung, T.-S. Lui, L.-H. Chen, J.-W. Huang, Effects of friction stir process and stabilizing heat treatment on the tensile and punch-shear properties of mg–9li–2al–1zn magnesium alloy, Materials transactions 54 (4) (2013) 505–511.

[35] S. Y. Betsofen, V. Antipov, M. Knyazev, Al–cu–li and al–mg–li alloys: Phase composition, texture, and anisotropy of mechanical properties, Russian Metallurgy (Metally) 2016 (4) (2016) 326–341.

[36] R. Rana, R. Purohit, S. Das, Reviews on the influences of alloying elements on the microstructure and mechanical properties of aluminum alloys and aluminum alloy composites, International Journal of Scientific and research publications 2 (6) (2012) 1–7.

[37] R. Islam, M. Haghshenas, Statistical optimization of stress level in mg-li-al alloys upon hot compression testing, Journal of Magnesium and Alloys 7 (2) (2019) 203–217.

[38] R. Islam, A. Hadadzadeh, M. Wells, M. Haghshenas, Characterization and analysis of hot compression behaviors of an ultralight mg-li-al alloy, International Journal of Lightweight Materials and Manufacture 2 (3) (2019) 217–226.

[39] C. Guo, F. Jiang, R. Wu, M. Zhang, Effect of strain rate on compressive mechanical properties of extruded mg–8li–1al–1ce alloy, Materials & Design 49 (2013) 110–115.

[40] A. Jain, S. P. Ong, G. Hautier, W. Chen, W. D. Richards, S. Dacek, S. Cholia, D. Gunter, D. Skinner, G. Ceder, K. a. Persson, The Materials Project: A materials genome approach to accelerating materials innovation, APL Materials 1 (1) (2013) 011002. `doi:10.1063/1.4812323`.
URL `http://link.aip.org/link/AMPADS/v1/i1/p011002/s1&Agg=doi`

[41] A. E92-16, Standard test methods for vickers hardness and knoop hardness of metallic materials, West Conshohocken, PA (2016).

[42] H. Li, P. Motamedi, J. Hogan, Characterization and mechanical testing on novel $(\gamma+ \ \alpha2)$–tial/ti3al/al2o3 cermet, Materials Science and Engineering: A 750 (2019) 152–163.

[43] W. Chen, G. Subhash, G. Ravichandran, Evaluation of ceramic specimen geometries used in a split hopkinson pressure bar, Dymat Journal 1 (3) (1994) 193–210.

[44] M. Pankow, C. Attard, A. Waas, Specimen size and shape effect in split hopkinson pressure bar testing, The Journal of Strain Analysis for Engineering Design 44 (8) (2009) 689–698.

[45] J. J. Swab, C. S. Meredith, D. T. Casem, W. R. Gamble, Static and dynamic compression strength of hot-pressed boron carbide using a dumbbell-shaped specimen, Journal of Materials Science 52 (17) (2017) 10073–10084.

[46] J. Swab, W. Chen, J. Hogan, H. Liao, C. Lo, S. Mates, C. Meredith, J. Pittari, R. Rhorer, G. Quinn, Dynamic compression strength of ceramics: What was learned from an interlaboratory round robin exercise?, Journal of Dynamic Behavior of Materials (2020) 1–14.

[47] H. Li, P. Motamedi, J. D. Hogan, On the rate-dependency of mechanical properties and failure mechanisms of a $(\gamma+ \ \alpha2)$-tial/ti3al-al2o3 cermet, Materials Science and Engineering: A 791 (2020) 139747.

[48] Y. Wang, D. Zhou, H. Liu, S. M. Zakir, Y. Li, Dynamic fracture process and strain rate effect of a porous sic ceramic, in: Multidisciplinary Digital Publishing Institute Proceedings, Vol. 2, 2018, p. 509.

[49] Z. Wang, R. Li, W. Song, Dynamic failure and inelastic deformation behavior of sic ceramic under uniaxial compression, Ceramics International 46 (1) (2020) 612–617.

[50] M. Shafiq, G. Subhash, Dynamic deformation characteristics of zirconium diboride–silicon carbide under multi-axial confinement, International Journal of Impact Engineering 91 (2016) 158–169.

[51] J. Chen, B. Guo, H. Liu, H. Liu, P. Chen, Dynamic brazilian test of brittle materials using the split hopkinson pressure bar and digital image correlation, Strain 50 (6) (2014) 563–570.

[52] F. Hild, A. Bouterf, P. Forquin, S. Roux, On the use of digital image correlation for the analysis of the dynamic behavior of materials, in: The micro-world observed by ultra high-speed cameras, Springer, 2018, pp. 185–206.

[53] C. Lo, T. Sano, J. D. Hogan, Microstructural and mechanical characterization of variability in porous advanced ceramics using x-ray computed tomography and digital image correlation, Materials Characterization 158 (2019) 109929.

[54] M. V. Canté, J. E. Spinelli, N. Cheung, A. Garcia, The correlation between dendritic microstructure and mechanical properties of directionally solidified hypoeutectic al-ni alloys, Metals and Materials International 16 (1) (2010) 39–49.

[55] G. A. Santos, C. de Moura Neto, W. R. Osório, A. Garcia, Design of mechanical properties of a zn27al alloy based on microstructure dendritic array spacing, Materials & design 28 (9) (2007) 2425–2430.

[56] H. Esaka, W. Kurz, Columnar dendrite growth: experiments on tip growth, Journal of crystal growth 72 (3) (1985) 578–584.

[57] X. Liao, Q. Zhai, J. Luo, W. Chen, Y. Gong, Refining mechanism of the electric current pulse on the solidification structure of pure aluminum, Acta Materialia 55 (9) (2007) 3103–3109.

[58] H. Hu, X. Nie, Y. Ma, Corrosion and surface treatment of magnesium alloys, Magnesium Alloys-Properties in Solid and Liquid States; Czerwinski, F., Ed (2014) 67–108.

[59] N. Goel, J. Cahoon, The al-li-mg system (aluminum-lithium-magnesium), Bulletin of Alloy Phase Diagrams 11 (6) (1990) 528–546.

[60] B. Dubost, P. Bompard, I. Ansara, Experimental study and thermodynamic calculation of the al-li-mg equilibrium phase diagram, Le Journal de Physique Colloques 48 (C3) (1987) C3–473.

[61] J. Liu, M. Kulak, A new paradigm in the design of aluminum alloys for aerospace applications, in: Materials Science Forum, Vol. 331, Trans Tech Publ, 2000, pp. 127–142.

[62] S. Kim, M. C. Jo, T. W. Park, J. Ham, S. S. Sohn, S. Lee, Correlation of dynamic compressive properties, adiabatic shear banding, and ballistic performance of high-strength 2139 and 7056 aluminum alloys, Materials Science and Engineering: A 804 (2021) 140757.

[63] A. Baroutaji, M. Sajjia, A.-G. Olabi, On the crashworthiness performance of thin-walled energy absorbers: recent advances and future developments, Thin-Walled Structures 118 (2017) 137–163.

[64] M. M. Avedesian, H. Baker, et al., ASM specialty handbook: magnesium and magnesium alloys, ASM international, 1999.

[65] Z. Chen, C. Bao, G. Wu, Y. Jian, Z. Huang, H. Ma, Effects of yal2 reinforced particles on the tribological properties of la143 alloy under dry sliding condition, Wear 438 (2019) 203077.

[66] D. W. Christianson, L. Zhu, M. V. Manuel, Experimental measurement of diffusion coefficients and assessment of diffusion mobilities in hcp mg–li–al alloys, Calphad 71 (2020) 101999.

[67] A. d. S. Scari, B. C. Pockszevnicki, J. Landre Junior, P. A. A. Magalhaes Junior, Stress-strain compression of aa6082-t6 aluminum alloy at room temperature, Journal of Structures 2014 (2014).

[68] M. Liu, L. Zhang, P. Wang, Y. Chang, Buckling behaviors of section aluminum alloy columns under axial compression, Engineering Structures 95 (2015) 127–137.

[69] F. M. Mazzolani, V. Piluso, G. Rizzano, Local buckling of aluminum alloy angles under uniform compression, Journal of Structural Engineering 137 (2) (2011) 173–184.

[70] M. Easton, W. Q. Song, T. Abbott, A comparison of the deformation of magnesium alloys with aluminium and steel in tension, bending and buckling, Materials & design 27 (10) (2006) 935–946.

[71] L. Jiang, J. J. Jonas, R. Mishra, A. Luo, A. Sachdev, S. Godet, Twinning and texture development in two mg alloys subjected to loading along three different strain paths, Acta Materialia 55 (11) (2007) 3899–3910.

[72] V. Kannan, K. Hazeli, K. Ramesh, The mechanics of dynamic twinning in single crystal magnesium, Journal of the Mechanics and Physics of Solids 120 (2018) 154–178.

[73] B. M. Koch, P. Jannotti, D. Mallick, B. Schuster, T. Sano, J. D. Hogan, Influence of microstructure on the impact failure of alumina, Materials Science and Engineering: A 770 (2020) 138549.

[74] E. Strassburger, H. Senf, Experimental investigations of wave and fracture phenomena in impacted ceramics and glasses., Tech. rep., Fraunhofer-Inst Fuer Kurzzeitdynamik-Ernst-Mach-Inst Weil Am Rhein (Germany) (1995).

[75] Z. Jun, D. Jianxin, Z. Jianhua, A. Xing, Failure mechanisms of a whisker-reinforced ceramic tool when machining nickel-based alloys, Wear 208 (1-2) (1997) 220–225.

[76] E. Misra, N. Theodore, J. Mayer, T. Alford, Failure mechanisms of pure silver, pure aluminum and silver–aluminum alloy under high current stress, Microelectronics Reliability 46 (12) (2006) 2096–2103.

[77] T. Guo, Y. Chen, R. Cao, X. Pang, J. He, L. Qiao, Cleavage cracking of ductile-metal substrates induced by brittle coating fracture, Acta Materialia 152 (2018) 77–85.

[78] R. Taghiabadi, A. Moharami, Mechanical properties enhancement of mg–4si in-situ composites by friction stir processing, Materials Science and Technology 37 (1) (2021) 66–77.

[79] Y.-S. Su, S.-X. Li, G.-N. Yang, F. Yu, S.-Y. Lu, Y.-G. Wang, Shear instability and considerably localized melting in quasi-static compression, Materials Characterization 160 (2020) 110081.

[80] Z. Yu, S. Tan, Z. Shan, X. Tian, X-ray computed tomography quantification of damage in concrete under compression considering irreversible mode-ii microcracks, Fatigue & Fracture of Engineering Materials & Structures 40 (12) (2017) 1960–1972.

[81] T. Jiao, Y. Li, K. Ramesh, A. Wereszczat, High rate response and dynamic failure of structural ceramics, International Journal of Applied ceramic technology 1 (3) (2004) 243–253.

[82] B. Paliwal, K. Ramesh, J. McCauley, Direct observation of the dynamic compressive failure of a transparent polycrystalline ceramic (alon), Journal of the American Ceramic Society 89 (7) (2006) 2128–2133.

[83] L. Farbaniec, J. Hogan, K. Ramesh, Micromechanisms associated with the dynamic compressive failure of hot-pressed boron carbide, Scripta Materialia 106 (2015) 52–56.

[84] C. Wang, Y. Xu, E. Han, Serrated flow and abnormal strain rate sensitivity of a magnesium–lithium alloy, Materials letters 60 (24) (2006) 2941–2944.

[85] L. Zhang, H. He, S. Li, X. Wu, L. Li, Dynamic compression behavior of 6005 aluminum alloy aged at elevated temperatures, Vacuum 155 (2018) 604–611.

[86] A. S. Khan, R. Liang, Behaviors of three bcc metal over a wide range of strain rates and temperatures: experiments and modeling, International Journal of Plasticity 15 (10) (1999) 1089–1109.

[87] Q. Wei, T. Jiao, K. Ramesh, E. Ma, Nano-structured vanadium: processing and mechanical properties under quasi-static and dynamic compression, Scripta materialia 50 (3) (2004) 359–364.

[88] R. Armstrong, S. Walley, High strain rate properties of metals and alloys, International Materials Reviews 53 (3) (2008) 105–128.

[89] J. Lankford, W. Predebon, J. Staehler, G. Subhash, B. Pletka, C. Anderson, The role of plasticity as a limiting factor in the compressive failure of high strength ceramics, Mechanics of Materials 29 (3-4) (1998) 205–218.

[90] C. Hustedt, P. Lambert, V. Kannan, E. Huskins-Retzlaff, D. Casem, M. Tate, H. Philipp, A. Woll, P. Purohit, J. Weiss, et al., In situ time-resolved measurements of extension twinning during dynamic compression of polycrystalline magnesium, Journal of Dynamic Behavior of Materials 4 (2) (2018) 222–230.

[91] F. Coghe, W. Tirry, L. Rabet, D. Schryvers, P. Van Houtte, Importance of twinning in static and dynamic compression of a ti–6al–4v titanium alloy with an equiaxed microstructure, Materials Science and Engineering: A 537 (2012) 1–10.

[92] A. Y. Kuksin, A. Yanilkin, Dislocation nucleation and motion in metals and alloys at high-rate deformation: molecular dynamic simulation, Mechanics of Solids 50 (1) (2015) 44–51.

[93] Q. Wei, S. Cheng, K. Ramesh, E. Ma, Effect of nanocrystalline and ultrafine grain sizes on the strain rate sensitivity and activation volume: fcc versus bcc metals, Materials Science and Engineering: A 381 (1-2) (2004) 71–79.

[94] A. A. Brown, D. J. Bammann, Validation of a model for static and dynamic recrystallization in metals, International Journal of Plasticity 32 (2012) 17–35.

[95] Z. Yang, Y. Guo, J. Li, F. He, F. Xia, M. Liang, Plastic deformation and dynamic recrystallization behaviors of mg–5gd–4y–0.5 zn–0.5 zr alloy, Materials Science and Engineering: A 485 (1-2) (2008) 487–491.

[96] R. Zhang, D. Wang, L. Huang, S. Yuan, L. Geng, Deformation behaviors and microstructure evolution of tibw/ta15 composite with novel network architecture, Journal of Alloys and Compounds 722 (2017) 970–980.

[97] P. Ponnusamy, S. Masood, D. Ruan, S. Palanisamy, R. Rashid, High strain rate dynamic behaviour of alsi12 alloy processed by selective laser melting, The International Journal of Advanced Manufacturing Technology 97 (1) (2018) 1023–1035.

[98] P. Ponnusamy, R. A. Rahman Rashid, S. H. Masood, D. Ruan, S. Palanisamy, Mechanical properties of slm-printed aluminium alloys: A review, Materials 13 (19) (2020) 4301.

[99] Y. Duan, B. Du, X. Shi, B. Hou, Y. Li, Quasi-static and dynamic compressive properties and deformation mechanisms of 3d printed polymeric cellular structures with kelvin cells, International Journal of Impact Engineering 132 (2019) 103303.

[100] M. Kucewicz, P. Baranowski, M. Stankiewicz, M. Konarzewski, P. Płatek, J. Małachowski, Modelling and testing of 3d printed cellular structures under quasi-static and dynamic conditions, Thin-Walled Structures 145 (2019) 106385.

[101] G. Bi, Z. Xu, J. Jiang, Y. Li, T. Chen, W. Fu, D. Fang, X. Ding, High-speed impact behavior and microstructure evolution of an extruded mg-7sn-5zn-3al alloy, Journal of Materials Engineering and Performance 29 (10) (2020) 6427–6438.

[102] B. Zhu, X. Liu, C. Xie, W. Liu, C. Tang, L. Lu, The flow behavior in as-extruded az31 magnesium alloy under impact loading, Journal of magnesium and alloys 6 (2) (2018) 180–188.

[103] R. Graça-e Costa, J. Alfaiate, D. Dias-da Costa, L. Sluys, A non-iterative approach for the modelling of quasi-brittle materials, International Journal of Fracture 178 (1-2) (2012) 281–298.

[104] P. Forquin, Brittle materials at high-loading rates: an open area of research (2017).

[105] M. Iskander, N. Shrive, Fracture of brittle and quasi-brittle materials in compression: a review of the current state of knowledge and a different approach, Theoretical and Applied Fracture Mechanics 97 (2018) 250–257.

[106] T. Wang, X. Ye, Z. Liu, D. Chu, Z. Zhuang, Modeling the dynamic and quasi-static compression-shear failure of brittle materials by explicit phase field method, Computational Mechanics 64 (6) (2019) 1537–1556.

[107] L. Weng, X. Li, A. Taheri, Q. Wu, X. Xie, Fracture evolution around a cavity in brittle rock under uniaxial compression and coupled static–dynamic loads, Rock Mechanics and Rock Engineering 51 (2) (2018) 531–545.

[108] L. Zhou, Z. Zhu, H. Qiu, X. Zhang, L. Lang, Study of the effect of loading rates on crack propagation velocity and rock fracture toughness using cracked tunnel specimens, International Journal of Rock Mechanics and Mining Sciences 112 (2018) 25–34.

[109] L. Pereira, J. Weerheijm, L. Sluys, A numerical study on crack branching in quasi-brittle materials with a new effective rate-dependent nonlocal damage model, Engineering Fracture Mechanics 182 (2017) 689–707.

[110] B. Lawn, Fracture of brittle solids, Cambridge university press, 1993.

[111] J. D. Hogan, L. Farbaniec, N. Daphalapurkar, K. Ramesh, On compressive brittle fragmentation, Journal of the American Ceramic Society 99 (6) (2016) 2159–2169.

[112] L. Farbaniec, J. Hogan, K. Xie, M. Shaeffer, K. Hemker, K. Ramesh, Damage evolution of hot-pressed boron carbide under confined dynamic compression, International Journal of Impact Engineering 99 (2017) 75–84.

[113] Q. B. Zhang, J. Zhao, A review of dynamic experimental techniques and mechanical behaviour of rock materials, Rock mechanics and rock engineering 47 (4) (2014) 1411–1478.

[114] H. Reinhardt, J. Weerheijm, Tensile fracture of concrete at high loading rates taking account of inertia and crack velocity effects, International Journal of Fracture 51 (1) (1991) 31–42.

[115] M. Wang, F. Wang, Z. Zhu, Y. Dong, M. Mousavi Nezhad, L. Zhou, Modelling of crack propagation in rocks under shpb impacts using a damage method, Fatigue & Fracture of Engineering Materials & Structures 42 (8) (2019) 1699–1710.

[116] A. Bertram, J. Kalthoff, Crack propagation toughness of rock for the range of low to very high crack speeds, in: Key engineering materials, Vol. 251, Trans Tech Publ, 2003, pp. 423–430.

[117] E. Strassburger, H. Senf, H. Rothenhäusler, Fracture propagation during impact in three types of ceramics, Le Journal de Physique IV 4 (C8) (1994) C8–653.

[118] E. Strassburger, Visualization of impact damage in ceramics using the edge-on impact technique, International Journal of Applied Ceramic Technology 1 (3) (2004) 235–242.

[119] C. Denoual, C. E. Cottenot, et al., Visualization of the damage evolution in impacted silicon carbide ceramics, International Journal of Impact Engineering 21 (4) (1998) 225–235.

[120] G. Y. Sha, Y. B. Xu, E. H. Han, Dynamic crack propagation behavior of the mg-li alloys under high-speed impact loading, in: Materials Science Forum, Vol. 488, Trans Tech Publ, 2005, pp. 717–720.

[121] D. Mallick, M. Zhao, J. Parker, V. Kannan, B. Bosworth, D. Sagapuram, M. Foster, K. Ramesh, Laser-driven flyers and nanosecond-resolved velocimetry for spall studies in thin metal foils, Experimental Mechanics 59 (5) (2019) 611–628.

[122] L. Farbaniec, C. Williams, L. Kecskes, R. Becker, K. Ramesh, Spall response and failure mechanisms associated with a hot-extruded amx602 mg alloy, Materials Science and Engineering: A 707 (2017) 725–731.

[123] G. Zhang, G. A. Gazonas, F. Bobaru, Supershear damage propagation and sub-rayleigh crack growth from edge-on impact: a peridynamic analysis, International Journal of Impact Engineering 113 (2018) 73–87.

[124] I. Asareh, T.-Y. Kim, J.-H. Song, A linear complete extended finite element method for dynamic fracture simulation with non-nodal enrichments, Finite Elements in Analysis and Design 152 (2018) 27–45.

[125] J. Bleyer, C. Roux-Langlois, J.-F. Molinari, Dynamic crack propagation with a variational phase-field model: limiting speed, crack branching and velocity-toughening mechanisms, International Journal of Fracture 204 (1) (2017) 79–100.

[126] L.-Y. Zhao, J.-F. Shao, Q.-Z. Zhu, Analysis of localized cracking in quasi-brittle materials with a micro-mechanics based friction-damage approach, Journal of the Mechanics and Physics of Solids 119 (2018) 163–187.

[127] S. Rahal, A. Sellier, G. Casaux-Ginestet, Finite element modelling of permeability in brittle materials cracked in tension, International Journal of Solids and Structures 113 (2017) 85–99.

[128] G. Lu, J. Chen, A new nonlocal macro-meso-scale consistent damage model for crack modeling of quasi-brittle materials, Computer Methods in Applied Mechanics and Engineering 362 (2020) 112802.

[129] P. Forquin, E. Ando, Application of microtomography and image analysis to the quantification of fragmentation in ceramics after impact loading, Philosophical Transactions of the Royal Society A: Mathematical, Physical and Engineering Sciences 375 (2085) (2017) 20160166.

[130] C. Lo, T. Sano, J. D. Hogan, Deformation mechanisms and evolution of mechanical properties in damaged advanced ceramics, Journal of the European Ceramic Society 40 (8) (2020) 3129–3139.

[131] X. Chen, A. H. Chan, Modelling impact fracture and fragmentation of laminated glass using the combined finite-discrete element method, International Journal of Impact Engineering 112 (2018) 15–29.

[132] T. K. Mandal, V. P. Nguyen, A. Heidarpour, Phase field and gradient enhanced damage models for quasi-brittle failure: A numerical comparative study, Engineering Fracture Mechanics 207 (2019) 48–67.

[133] G. T. Camacho, M. Ortiz, Computational modelling of impact damage in brittle materials, International Journal of solids and structures 33 (20-22) (1996) 2899–2938.

[134] D. Halm, A. Dragon, An anisotropic model of damage and frictional sliding for brittle materials, European Journal of Mechanics-A/Solids 17 (3) (1998) 439–460.

[135] X. Lai, L. Liu, S. Li, M. Zeleke, Q. Liu, Z. Wang, A non-ordinary state-based peridynamics modeling of fractures in quasi-brittle materials, International Journal of Impact Engineering 111 (2018) 130–146.

[136] L.-Y. Zhao, Q.-Z. Zhu, J.-F. Shao, A micro-mechanics based plastic damage model for quasi-brittle materials under a large range of compressive stress, International Journal of Plasticity 100 (2018) 156–176.